RAPID AND ROBUST IMAGE RECONSTRUCTION FOR MAGNETIC PARTICLE IMAGING

A THESIS SUBMITTED TO
THE GRADUATE SCHOOL OF ENGINEERING AND SCIENCE
OF BILKENT UNIVERSITY
IN PARTIAL FULFILLMENT OF THE REQUIREMENTS FOR
THE DEGREE OF
MASTER OF SCIENCE
IN
ELECTRICAL AND ELECTRONICS ENGINEERING

By
Semih Kurt
June 2020

RAPID AND ROBUST IMAGE RECONSTRUCTION
FOR MAGNETIC PARTICLE IMAGING
By Semih Kurt
June 2020

We certify that we have read this thesis and that in our opinion it is fully adequate, in scope and in quality, as a thesis for the degree of Master of Science.

Emine Ülkü Sarıtaş Çukur(Advisor)

Tolga Çukur

Behçet Murat Eyüboğlu

Approved for the Graduate School of Engineering and Science:

Ezhan Karaşan
Director of the Graduate School

ABSTRACT

RAPID AND ROBUST IMAGE RECONSTRUCTION FOR MAGNETIC PARTICLE IMAGING

Semih Kurt
M.S. in Electrical and Electronics Engineering
Advisor: Emine Ülkü Sarıtaş Çukur
June 2020

Magnetic Particle Imaging (MPI) is a rapidly developing medical imaging modality, which can image with high resolution, contrast, and sensitivity the spatial distribution of superparamagnetic iron oxide nanoparticles. Several applications of MPI have been introduced on angiography, cancer imaging, and stem cell tracking. Due to the safety limits on time-varying magnetic fields, MPI images are obtained by dividing the field-of-view (FOV) into numerous relatively small partial FOVs (pFOVs). Each pFOV suffers from a DC loss due to direct feedthrough interference caused by simultaneous excitation and signal reception. The standard x-space image reconstruction first processes each pFOV separately, and then combines them by enforcing smoothness and non-negativity constraints on the final image. These steps require the pFOVs to overlap, and can amplify the effects of non-ideal signal conditions, such as harmonic interference, noise, and nanoparticle relaxation. This thesis proposes two robust x-space image reconstruction techniques. The first technique, pFOV center imaging (PCI), first forms a raw image of the entire FOV by directly mapping the signal to pFOV centers. The final image is then reconstructed by deconvolving this raw image with a known, compact kernel. The second technique, harmonic dispersion x-space (HD-X), takes advantage of the dispersion in signal harmonics in the case of rapid scan trajectories. Followed by a sharp bandstop filtering of the fundamental harmonic, this technique directly grids the signal to form the final image, and does not require overlapping pFOVs. PCI offers robustness against harmonic interferences, and HD-X enables x-space reconstruction of rapid and sparse trajectories with non-overlapping pFOVs. Extensive simulations and imaging experiments show that both proposed methods outperform standard x-space reconstruction in terms of robustness against non-ideal signal conditions and image quality.

Keywords: magnetic particle imaging, image reconstruction, robustness.

ÖZET

MANYETİK PARÇACIK GÖRÜNTÜLEME İÇİN HIZLI VE GÜRBÜZ GÖRÜNTÜ GERİÇATIMI

Semih Kurt
Elektrik ve Elektronik Mühendisliği, Yüksek Lisans
Tez Danışmanı: Emine Ülkü Sarıtaş Çukur
Haziran 2020

Manyetik Parçacık Görüntüleme (MPG) süperparamanyetik demir oksit nanoparçacıklarının uzamsal dağılımlarını yüksek çözünürlük, kontrast ve hassasiyetle görüntüleyen, ve hızla gelişen bir medikal görüntüleme tekniğidir. MPG, anjiyografi, kanser görüntüleme ve kök hücre takibi gibi uygulamalara sahiptir. Alternatif manyetik alanların güvenlik sınırları nedeniyle, MPG görüntüleri görüş alanını (GA) çok sayıda görece küçük kısmi GA'lara (kGA) bölerek elde edilir. Eşzamanlı uyarım ve sinyal alımının neden olduğu geribeslemeden dolayı, her bir kGA sabit bir değer kaybı yaşar. Standart x-uzayı görüntü geriçatımı her bir kGA'yı tek başına işledikten sonra, son görüntüde negatif olmama ve süreklilik kısıtlarını zorlayarak tüm kGA'ları birleştirir. Bu işlemler kGA'ların örtüşmesini gerektirir, ve harmonik girişim, gürültü, nanoparçacık relaksasyonu gibi ideal olmayan sinyal koşullarının etkilerini artırabilir. Bu tezde iki farklı gürbüz x-uzayı görüntü geriçatım tekniği önerilmektedir. kGA merkez görüntüleme (KMG) ismindeki ilk teknik, öncelikle sinyali doğrudan kGA merkezlerine atayarak tüm GA'nın ham bir görüntüsünü oluşturur. Son MPG görüntüsü ise bu ham görüntünün bilinen ve kompakt bir çekirdekle ters evrişimi ile geriçatılır. Harmonik dağılım x-uzayı (HD-X) ismindeki ikinci teknik ise hızlı tarama gezingeleri için sinyal harmoniklerinin dağılımından faydalanır. Bu teknik, temel harmonikte keskin bir bant söndüren süzgeci takiben MPG sinyalini doğrudan gridleyerek son görüntüyü oluşturur, ve kGA'ların örtüşmesini gerektirmez. KMG harmonik girişimlere karşı gürbüzlük sağlarken, HD-X örtüşmeyen kGA'lar içeren hızlı ve seyrek gezingelerin x-uzayı geriçatımlarını mümkün kılar. Kapsamlı benzetimler ve görüntüleme deneyleri, önerilen her iki tekniğin de ideal olmayan sinyal koşullarına karşı gürbüzlük ve görüntü kalitesi açısından standart x-uzayı geriçatımından üstün olduğunu göstermektedir.

Anahtar sözcükler: manyetik parçacık görüntüleme, görüntü geriçatımı, gürbüzlük.

Acknowledgement

First of all, I would like to express my deep gratitude to my advisor, Asst. Prof. Emine Ülkü Sarıtaş, for all the support and encouragement she gave me throughout my graduate years. She always motivated me and showed the right direction, whenever I needed. I feel privileged to have her as the advisor for my master studies. I am thankful to her for her belief in me.

I would also like to thank Assoc. Prof. Tolga Çukur and Prof. Behçet Murat Eyüboğlu for giving valuable feedback and being a member of my thesis committee.

I would like to thank the following funding agencies for supporting the work in this thesis: the Scientific and Technological Research Council of Turkey through TUBITAK Grants 115E677 and 217S069, the European Commission through FP7 Marie Curie Career Integration Grant (PCIG13-GA-2013-618834), the Turkish Academy of Sciences through TUBA-GEBIP 2015 program, and the BAGEP Award of the Science Academy.

I am grateful to my lab members Ecrin Yağız, Mustafa Ütkür, Abdullah Ömer Arol, Ahmet Rahmetullah Çağıl, Yavuz Muslu, and Musa Tunç Arslan for their helps on my work. I want to thank to my friends Yiğit, Emir, and Alican for their efforts to keep me motivated throughout my master studies.

Finally, I want to thank to my parents for all their supports.

Contents

List of Figures

Chapter 1

Introduction

Magnetic Particle Imaging (MPI) leverages the nonlinear magnetization response of superparamagnetic iron oxide (SPIO) nanoparticles, to generate an image of their spatial distribution with high resolution, contrast, and sensitivity [1, 2, 3, 4, 5, 6]. Three different magnetic fields are utilized to obtain the MPI signal. A static selection field with a strong gradient creates a field free point (FFP). A sinusodial drive field excites the nanoparticles in the vicinity of the FFP, effectively scanning a field-of-view (FOV) via moving the FFP. However, safety limits restrict the size of the FOV that can be scanned by the drive field alone to a few cm or less [7, 8]. The small FOV covered by the drive field is called a partial FOV (pFOV) [9] or a patch [10, 11, 12]. Then, to cover larger FOVs, low-frequency focus fields are employed [13]. Due to the limits on the slew rates of the focus fields [14, 8], a realistic scan trajectory may consist of numerous highly-overlapping small pFOVs. In x-space reconstruction, these pFOVs are first individually processed by gridding the speed-compensated signal to the trajectory of the FFP, and then combined to form the image of the entire FOV [15, 16, 9, 17, 18, 19]. The resulting MPI image shows the spatial distribution of the nanoparticles blurred by the point spread function (PSF) of the imaging system.

One of the challenges in MPI is the direct feedthrough signal caused by the simultaneous excitation and reception, as it can be many orders of magnitude larger than the nanoparticle signal [15, 16]. To keep the direct feedthrough contained to the fundamental harmonic, the drive field is typically chosen as a pure sinusoid. Then, a gradiometric receive coil [20, 21, 22], active/passive compensation [23], and/or analog/digital filtering can be utilized to counteract the effects of the direct feedthrough. During image reconstruction with the x-space approach, the fundamental harmonic lost due to filtering is recovered via enforcing smoothness and non-negativity on the reconstructed image [9, 24]. A 3D extension of this approach was also formulated as a convex optimization problem, ensuring the consistency of the recovered information across pFOVs [17].

The standard x-space reconstruction first processes MPI signals for different pFOVs individually to form pFOV images [15]. These processing steps on individual pFOVs include speed compensation and gridding of the MPI signal to the FFP positions. The final pFOV images have different DC losses stemming from the fundamental harmonic lost due to the direct feedthrough filtering. Next, these pFOV images with DC losses are combined to form the image of the entire FOV based on the smoothness and non-negativity prior of the final image [9]. To enforce smoothness, standard x-space reconstruction requires the pFOVs to overlap.. Accordingly, the DC losses are recovered in such a way that the overlapping regions of the pFOV images agree with each other. However, the above-mentioned steps can render x-space reconstruction sensitive to non-ideal signal conditions, such as harmonic interference, noise, and relaxation effects. Moreover, the requirement of overlapping pFOVs prohibits the x-space reconstructions of rapid and sparse trajectories with non-overlapping pFOVs.

This thesis proposes two robust x-space image reconstruction techniques. The first technique, pFOV center imaging (PCI), provides a robust reconstruction against non-ideal signal conditions via using the centers of the pFOVs and bypassing the individual pFOV processing steps. This technique consists of two steps: forming a raw image by directly mapping the MPI signal to pFOV centers and deconvolving this raw image by a known, compact kernel to obtain the final

reconstructed image. The results of imaging experiments and extensive simulations show that the proposed method outperforms standard x-space reconstruction in terms of both robustness against non-ideal signal conditions and image quality. The second technique, harmonic dispersion x-space (HD-X), solves the problem of x-space image reconstruction from trajectories with non-overlapping pFOVs. This streamlined method also simplifies the reconstruction process substantially: following a sharp bandstop filtering of the fundamental harmonic, the signal is periodically sampled and gridded to the FFP trajectory. Simulations and imaging experiments demonstrate that the proposed technique outperforms standard x-space reconstruction in terms of image quality for trajectories with overlapping pFOVs, while enabling x-space reconstruction of trajectories with non-overlapping pFOVs.

Chapter 2

Principles of Magnetic Particle Imaging

2.1 1D Signal Equations

MPI uses a static selection field with a strong gradient to create a FFP, and a sinusoidal drive field to excite nanoparticles and move the FFP (see Fig. 2.1). The nanoparticles in the vicinity of the FFP respond to the applied drive field, whereas other nanoparticles are in magnetic saturation and therefore cannot respond [1, 2]. The time-varying magnetization responses of the nanoparticles are then picked up inductively by the receive coils.

For the 1D case, assuming a static selection field superimposed with a sinusoidal drive field, the magnetic field at position x, $H(x,t)$, can be written as [15]:

$$H(x,t) = H_0(t) - Gx \tag{2.1}$$

Here, $-G\,[A/m/m]$ is the gradient of the selection field and $H_0(t)\,[A/m]$ is the drive field. The FFP position, $x_s(t)$, can then be found by solving $H(x,t) = 0$ for x, i.e.,

$$x_s(t) = G^{-1}H_0(t) \tag{2.2}$$

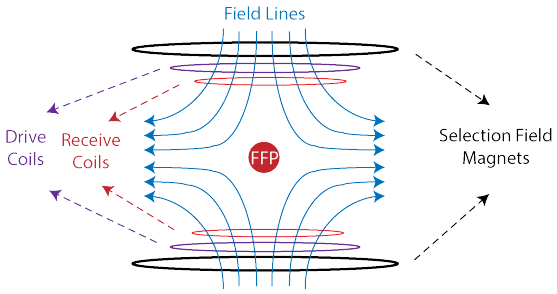

Figure 2.1: The selection field creates a FFP in space. Only those nanoparticles that are in the vicinity of the FFP respond to the applied drive field. This response is then picked up inductive receive coils.

The magnetic field at position x can be rewritten as:

$$H(x,t) = G\big(x_s(t) - x\big) \tag{2.3}$$

The magnetization of nanoparticles, M, in response to external magnetic field H can be formulated as follows:

$$M(H) = m\rho\mathcal{L}\left[kH\right] \tag{2.4}$$

where $m\,[Am^2]$ is the magnetic moment, ρ is the nanoparticle density, k is a property of the nanoparticle, and $\mathcal{L}\left[\cdot\right]$ is the Langevin function. By assuming a 1D distribution of nanoparticle density, $\rho(x)$, the time-varying magnetization response can be written as:

$$M(x,t) = m\rho(x)\delta(y)\delta(z)\mathcal{L}\left[kG\big(x_s(t) - x\big)\right] \tag{2.5}$$

Assuming it is picked-up by an inductive coil with the sensitivity $-B_1\,[T/A]$, the MPI signal can then be derived as follows:

$$\begin{aligned}
s(t) &= \int_V B_1 \frac{\partial M(\mathbf{x},t)}{\partial t} dV && \text{(2.6a)}\\
&= B_1 \frac{\partial}{\partial t} \int_V M(\mathbf{x},t) dV && \text{(2.6b)}\\
&= B_1 \frac{\partial}{\partial t} \int\int\int_S m\rho(u)\delta(v)\delta(w)\mathcal{L}\left[kG\big(x_s(t) - u\big)\right] dudvdw && \text{(2.6c)}\\
&= B_1 \frac{\partial}{\partial t} \big(m\rho(x) * \mathcal{L}\left[kGx\right]\big)\big|_{x=x_s(t)} && \text{(2.6d)}\\
&= B_1 mkG\dot{x}_s(t)\big(\rho(x) * h(x)\big)\big|_{x=x_s(t)} && \text{(2.6e)}
\end{aligned}$$

where

$$h(x) = \dot{\mathcal{L}}\left[kGx\right] \tag{2.7}$$

2.2 X-space Image Reconstruction

In standard x-space image reconstruction, the MPI signal is first divided by the FFP speed and other extra terms, to leave the particle distribution and $h(x)$ alone in convolution form [15, 9], i.e.,

$$IMG\big(x_s(t)\big) = \frac{s(t)}{B_1 mkG\dot{x}_s(t)} \tag{2.8a}$$

$$= \rho(x) * h(x)\big|_{x=x_s(t)} \tag{2.8b}$$

Then, the speed compensated signal is gridded to the equidistant positions in space. The resulting image shows the spatial distribution of nanoparticles convolved with a point spread function (PSF). As seen from Eqs. 2.7 and 2.8b, the PSF of the system, $h(x)$, is denoted by the derivative of the Langevin curve, which depends on both the selection field of the MPI scanner and the nanoparticle characteristics.

Due to the safety limits on the drive field, the size of the FOV that can be directly scanned by the drive field is restricted to a few cm's [7, 8]. Therefore, slow-varying focus fields are introduced to cover larger FOVs. Again, due to the safety limits on the slew rates of focus fields, a typical scan trajectory consists of numerous overlapping pFOVs. Standard x-space reconstruction first handles each pFOV individually as in Eq. 2.8b. Then, the pFOV images are combined to form the image of a larger FOV.

One of the important problems in MPI signal processing is the direct feedthrough due to the simultaneous excitation and reception. To eliminate this interference, the received MPI signal is high-pass filtered (see Fig. 2.2). This filtering also removes the first harmonic of the MPI signal.

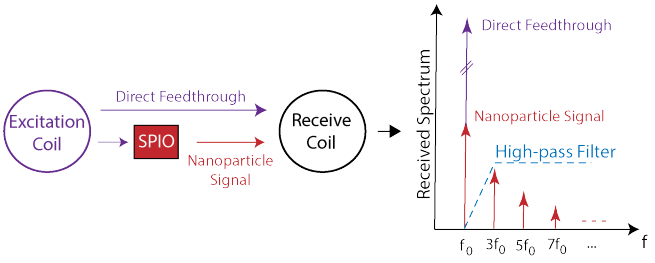

Figure 2.2: Direct feedthrough problem due to the simultaneous excitation and reception. The classical approach to solve this problem is to high-pass filter the received signal.

To understand the effect of this filtering, the received MPI signal can be written as a Fourier series [25, 9]:

$$s(t) = \sum_{n=1}^{\infty} S_n sin(2n\pi f_0 t) \tag{2.9}$$

where S_n is the Fourier coefficient of the n^{th} harmonic signal. Assuming $x_s(t) = Wcos(2\pi f_0 t)$, the x-space reconstruction method can be applied to the individual harmonics to derive the contributions of each harmonic to the image [9]:

$$\frac{s(t)}{B_1 mkG\dot{x}_s(t)}\bigg|_{t=\frac{1}{(2\pi f_0)}arccos(\frac{2x}{W})} = \alpha \sum_{n=1}^{\infty} S_n \frac{sin(2n\pi f_0 t)}{sin(2\pi f_0 t)}\bigg|_{t=\frac{1}{(2\pi f_0)}arccos(\frac{2x}{W})} \tag{2.10a}$$

$$= \alpha \sum_{n=1}^{\infty} S_n \frac{sin(n\ arccos(\frac{2x}{W}))}{sin(arccos(\frac{2x}{W}))} \tag{2.10b}$$

$$= \alpha \sum_{n=1}^{\infty} S_n U_{n-1}(\frac{2x}{W}) \tag{2.10c}$$

Here, W is the extent of each pFOV and α is a constant that depends on nanoparticle properties and scanning parameters. In addition, $U_{n-1}(x)$ are Chebyshev polynomials of the second kind (see Fig. 2.3). This equation shows that Chebyshev polynomials can be considered as a harmonic image basis set for MPI: the image contribution of the n^{th} harmonic is a Chebyshev polynomial weighted by the n^{th} Fourier coefficient, S_n. Importantly, because $U_0(x) = 1$, the first harmonic image corresponds to a constant. Therefore, the lost first harmonic signal causes a DC loss, which is different for each pFOV.

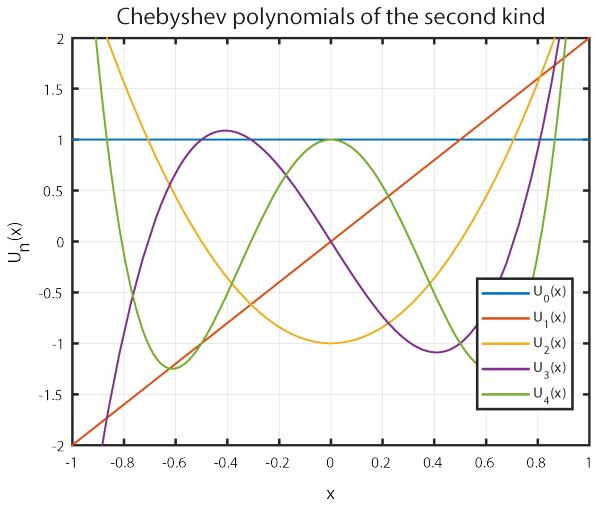

Figure 2.3: Chebyshev polynomials of the second kind form a harmonic image basis set for MPI.

In standard x-space reconstruction, each filtered pFOV signal is processed individually as in Eq. 2.8a to form the corresponding image. These pFOV images have different DC losses due to the lost first harmonic (see Fig. 2.4a). Next, the pFOVs are stitched to form the image of the entire FOV. During the pFOV stitching process, the DC losses are recovered via enforcing the smoothness and non-negativity of the final image (Fig. 2.4b).

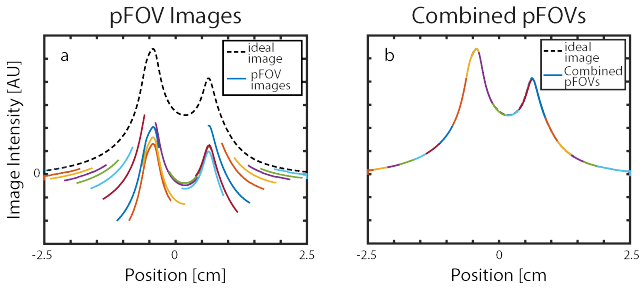

Figure 2.4: Standart x-space reconstruction. (a) pFOV images obtained via processing each pFOV individually, each having different DC losses due to the direct feedthrough filtering. (b) The stitching of pFOV images by enforcing the smoothness and non-negativity of the final image.

2.3 Multidimensional Signal Equations

In the multidimensional case, the received MPI signal can be written as [16]:

$$s(t) = \mathbf{B_1}(\mathbf{x}) m\rho(\mathbf{x}) * * * k\left\|\dot{\mathbf{x}}_\mathbf{s}\right\| \mathbf{h}(\mathbf{x})\hat{\dot{\mathbf{x}}}_\mathbf{s}\Big|_{x=\mathbf{x_s}(t)} \tag{2.11}$$

where $* * *$ denotes 3D convolution operation and

$$\mathbf{h}(\mathbf{x}) = \dot{\mathcal{L}}\big(k\|\mathbf{Gx}\|\big)\frac{\mathbf{Gx}}{\|\mathbf{Gx}\|}\left[\frac{\mathbf{Gx}}{\|\mathbf{Gx}\|}\right]^T\mathbf{G} + \frac{\mathcal{L}\big(k\|\mathbf{Gx}\|\big)}{k\|\mathbf{Gx}\|}\left(\mathbf{I} - \frac{\mathbf{Gx}}{\|\mathbf{Gx}\|}\left[\frac{\mathbf{Gx}}{\|\mathbf{Gx}\|}\right]^T\right)\mathbf{G} \tag{2.12}$$

Here, $\mathbf{x}$ is the position vector, $\mathbf{G}$ is the selection field gradient vector, $\mathbf{B_1}$ is the sensitivity vector, $\hat{\dot{\mathbf{x}}}_\mathbf{s}(t)$ is the unit vector along the direction of the FFP velocity vector $\dot{\mathbf{x}}_\mathbf{s}(t)$, and $\mathbf{h}(\mathbf{x})$ is the PSF for multidimensional x-space MPI. While the PSF is more complicated in this case, the reconstruction process follows the same speed compensation and gridding steps as in the 1D case.

Chapter 3

Partial FOV Center Imaging (PCI): A Robust X-Space Image Reconstruction for MPI

This chapter is based on the publication titled "Partial FOV Center Imaging (PCI): A Robust X-Space Image Reconstruction for Magnetic Particle Imaging", S. Kurt, Y. Muslu, E.U. Saritas, IEEE Transactions on Medical Imaging, DOI: 10.1109/TMI.2020.2995410.

3.1 Introduction

As explained in Chapter 2.2, the MPI signal is typically high-pass filtered to avoid the direct feedthrough signal. If the received signal also contains higher harmonics due to system non-idealities and/or interferences, however, simple filtering no longer suffices. In practice, therefore, a background measurement is subtracted from the received signal to cancel out potential higher harmonic interferences. If the interference level is comparable to the nanoparticle signal, or if there is a drift in the system, this background cancellation may not work as desired.

While the aforementioned x-space reconstruction techniques enforced consistency, smoothness and non-negativity, a detailed analysis on the detrimental effects of higher harmonic interference on the quality of the reconstructed MPI image has not yet been presented.

This chapter of the thesis presents a robust x-space image reconstruction technique called "pFOV center imaging" (PCI), which features substantially simplified pFOV processing and increased robustness against harmonic interferences. The proposed technique first forms a raw image of the entire FOV by mapping the MPI signal directly to the pFOV center locations. Then, this raw image is deconvolved by a fully known, compact kernel to obtain the corresponding MPI image. Importantly, the shape of this kernel solely depends on the pFOV size, and is independent of the other scanning parameters or the nanoparticle type. The performance of the proposed method was analyzed at different signal-to-noise ratio (SNR) and harmonic interference levels, demonstrating a trade-off between noise robustness and harmonic interference robustness. Extensive simulations, as well as imaging experiments on a FFP scanner, show that PCI outperforms standard x-space reconstruction in terms of image quality, noise robustness, and interference robustness.

3.2 Theory

For a trajectory that contains a 1D drive field superimposed with a slowly varying focus field, the pFOV centers are closely spaced and the FFP speed is dominated by the drive field. For such a trajectory, the time-domain MPI signal, $s\left(t\right)$, can be written as [15, 16]:

$$s\left(t\right) = \alpha \dot{x}_s\left(t\right) \hat{\rho}\big(x_s\left(t\right)\big) \tag{3.1}$$

where

$$\hat{\rho}\big(x_s\left(t\right)\big) = \rho\left(x\right) * h\left(x\right)\Big|_{x=x_s(t)} \tag{3.2}$$

Here, $x_s(t)$ is the instantaneous FFP position, $\dot{x}_s(t)$ is the instantaneous FFP speed, $\rho(x)$ is the particle distribution, $h(x)$ is the PSF, and $\hat{\rho}(x)$ is the PSF-blurred "ideal" MPI image. In addition, α is a constant that depends on the selection field gradient, the nanoparticle type, the magnetic moment of the nanoparticle, and the sensitivity of the receive coil [15, 16]. For the following derivations, the nanoparticle relaxation effects on the signal are ignored.

Due to direct feedthrough filtering, the MPI signal loses its fundamental harmonic component. It has been shown that the contribution of the lost first harmonic for each pFOV is a DC term [25, 9]. In standard x-space reconstruction, DC terms are recovered via pFOV stitching by enforcing non-negativity and continuity constraints on the reconstructed image [9].

3.2.1 Partial FOV Center Imaging (PCI):

Let x_{0j} be the center position of the j^{th} pFOV and t_{0j} be the time instant when the FFP is at x_{0j}, i.e.,

$$x_s(t)\Big|_{t=t_{0j}} = x_{0j} \quad , \text{ for } j = 1, ..., N \tag{3.3}$$

where N is the total number of pFOVs. Sampling $s(t)$ at the centers of pFOVs to get a raw image $\hat{\rho}_0(x)$ such that

$$\hat{\rho}_0(x_{0j}) = s(t)\Big|_{t=t_{0j}} \tag{3.4a}$$

$$= \alpha \dot{x}_s(t_{0j})\,\hat{\rho}(x_{0j}) \tag{3.4b}$$

$$= \beta_0 \hat{\rho}(x_{0j}) \quad , \text{ for } j = 1, ..., N \tag{3.4c}$$

For the trajectories considered here, because the FFP speed is dominated by the drive field, it can be considered as identical at the centers of pFOVs. Therefore, $\beta_0 = \alpha \dot{x}_s(t_{0j})$ is a constant for $j = 1, ..., N$.

In practice, due to direct feedthrough filtering, $\hat{\rho}_0(x)$ is devoid of the contribution of the first harmonic. It has been previously shown that the lost DC term

for the j^{th} pFOV can be represented by a convolution as [26]:

$$\hat{\rho}_{dc}\left(x_{0j}\right) = \frac{4}{\pi W}\left(\hat{\rho}\left(x\right) * \sqrt{1-\left(\frac{2x}{W}\right)^2}\right)\Bigg|_{x=x_{0j}} \tag{3.5}$$

where W is the extent of each pFOV. Note that while this expression was originally derived for stepped focus fields, it also applies when the focus fields are slowly varying. Taking into account the lost DC term and using Eqs. 3.4c and 3.5, the raw image at x_{0j} can be expressed as

$$\tilde{\rho}_0\left(x_{0j}\right) = \beta_0\big(\hat{\rho}\left(x_{0j}\right) - \hat{\rho}_{dc}\left(x_{0j}\right)\big) \tag{3.6a}$$

$$= \beta_0\left(\hat{\rho}\left(x\right) * \left(\delta\left(x\right) - \frac{4}{\pi W}\sqrt{1-\left(\frac{2x}{W}\right)^2}\right)\right)\Bigg|_{x=x_{0j}} \tag{3.6b}$$

valid for all $j = 1, ..., N$. Hence, the raw image $\tilde{\rho}_0\left(x\right)$ can be written as the ideal image convolved with a kernel, i.e.,

$$\tilde{\rho}_0\left(x\right) = \hat{\rho}\left(x\right) * h_0\left(x\right) \tag{3.7}$$

where

$$h_0\left(x\right) = \beta_0\left(\delta\left(x\right) - \frac{4}{\pi W}\sqrt{1-\left(\frac{2x}{W}\right)^2}\right) \tag{3.8}$$

Note that $h_0(x)$ is a compact kernel with full-width W, and is fully known up to a scaling factor β_0. Importantly, the shape of the kernel does not depend on the nanoparticle type. Next, $\tilde{\rho}_0\left(x\right)$ can be deconvolved by the known kernel $h_0(x)$ to obtain $\hat{\rho}(x)$, i.e.,

$$\hat{\rho}\left(x\right) = \tilde{\rho}_0\left(x\right) *^{-1} h_0\left(x\right) \tag{3.9}$$

Here, $*^{-1}$ denotes the deconvolution operation. This technique is called as pFOV center imaging (PCI).

Because PCI utilizes only the signals at pFOV centers, it is particularly robust against harmonic interference effects. This robustness is directly related to the MPI harmonic image basis set, which is composed of Chebyshev polynomials of the second kind [25, 9]. Independent of the harmonic number, each image basis varies relatively slowly near the pFOV centers when compared to locations

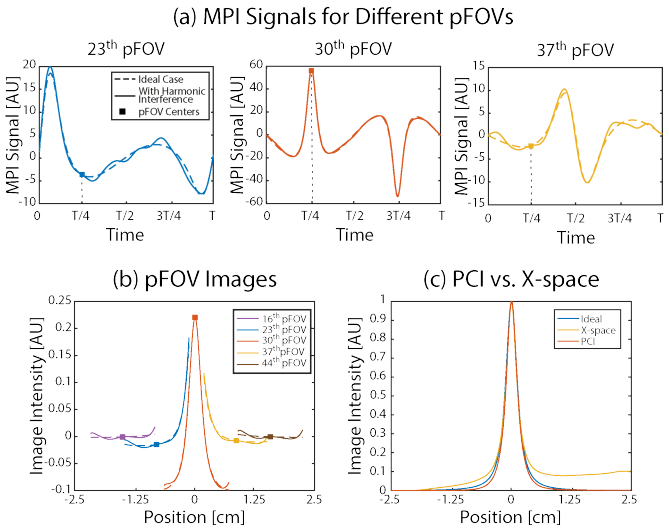

Figure 3.1: Effects of harmonic interference on the MPI signal and image reconstruction. (a) The signals after direct feedthrough filtering and (b) the reconstructed images from selected pFOVs with and without harmonic interference. The centers of pFOVs are particularly robust against interferences, while the edges can exhibit large deviations. (c) The reconstructed MPI images for PCI vs. standard x-space reconstruction. Standard x-space reconstruction exhibits an accumulated error toward one end of the image,while PCI image is free from such artifacts. Here, the ideal case refers to the convolution of the nanoparticle distribution with the imaging PSF. These simulations were performed for a point source placed at the origin, with 2.4 T/m/μ_0 gradient, 10 mT drive field at 9.7 kHz, 10 T/s slew-rate.

towards the edges. In return, the pFOV centers are particularly robust against harmonic interference effects, whereas the edges are sensitive to such interferences. A pictorial depiction of this effect is demonstrated in Fig. 3.1, where the MPI signal and corresponding images from different pFOVs are shown with and without harmonic interference (see Chapter 3.3.2 for details on these simulations). As seen Fig. 3.1a-b, the MPI signals and pFOV images corresponding to the pFOV centers are approximately the same with and without interference, whereas other positions can exhibit large deviations. These deviations make it more difficult to estimate the lost DC term, causing standard x-space reconstruction to exhibit an accumulated error toward one end of the image, as shown in Fig. 3.1c. On the other hand, the MPI image reconstructed using PCI does not exhibit such an artifact.

3.2.2 Lumped PCI:

Since PCI uses only a small portion of the received signal, it may be affected by noise. To increase robustness against noise, PCI can be modified to use all the received signal. Let x_{kj} be the k^{th} sampling position in the j^{th} pFOV and t_{kj} be the time instant when the FFP is at x_{kj}, i.e.,

$$x_s(t)\Big|_{t=t_{kj}} = x_{kj} \quad , \text{ for } j = 1, ..., N, \qquad k = -K, ..., K \tag{3.10}$$

where $2K+1$ is the number of samples in one half drive field cycle. A raw image $\hat{\rho}_k(x)$ can be constructed by sampling $s(t)$ at positions x_{kj}, but assigning these samples to center positions x_{0j}:

$$\hat{\rho}_k(x_{0j}) = \alpha \dot{x}_s(t_{kj})\, \hat{\rho}(x_{kj}) \tag{3.11a}$$

$$= \beta_k \hat{\rho}(x_{kj}) \tag{3.11b}$$

Note that the FFP speed is identical at the k^{th} sampling positions of pFOVs. Therefore $\beta_k = \alpha \dot{x}_s(t_{kj})$ is a constant for $j = 1, ..., N$.

Direct feedthrough filtering causes the same DC loss at all positions in a given FOV [9, 26]. Hence, similar to Eq. 3.6a, the raw image with lost DC term can be expressed as

$$\tilde{\rho}_k(x_{0j}) = \beta_k\big(\hat{\rho}(x_{kj}) - \hat{\rho}_{dc}(x_{0j})\big) \tag{3.12}$$

valid for all $j = 1, ..., N$. By comparing Eqs. 3.6a and 3.12,

$$\tilde{\rho}_k(x_{0j}) = \beta_k\Big(\hat{\rho}(x) * \delta\big(x - (x_{0j} - x_{kj})\big)\Big|_{x=x_{0j}} - \hat{\rho}_{dc}(x_{0j})\Big) \tag{3.13a}$$

$$= \beta_k\Bigg(\hat{\rho}(x) * \Bigg(\delta(x - (x_{0j} - x_{kj})) - \frac{4}{\pi W}\sqrt{1 - \left(\frac{2x}{W}\right)^2}\Bigg)\Bigg)\Bigg|_{x=x_{0j}} \tag{3.13b}$$

One can rewrite the k^{th} raw image $\tilde{\rho}_k(x)$ in a simplified form:

$$\tilde{\rho}_k(x) = \hat{\rho}(x) * h_k(x) \tag{3.14}$$

where

$$h_k(x) = \beta_k \left(\delta(x - (x_{0j} - x_{kj})) - \frac{4}{\pi W} \sqrt{1 - \left(\frac{2x}{W}\right)^2} \right) \tag{3.15}$$

Then, one can reconstruct $\hat{\rho}(x)$ via deconvolving $\tilde{\rho}_k(x)$ by $h_k(x)$:

$$\hat{\rho}(x) = \tilde{\rho}_k(x) *^{-1} h_k(x) \tag{3.16}$$

Eq. 3.14 shows that sampling $s(t)$ at different positions in pFOVs can create different raw images, and one can obtain $\hat{\rho}(x)$ from any of these raw images. Note that among all $\tilde{\rho}_k(x)$, the one with the highest SNR is $\tilde{\rho}_0(x)$, as the FFP speed is maximum when passing through the pFOV center. To boost the SNR and use the entire signal, one can sum all $\tilde{\rho}_k(x)$ to get a raw lumped image, i.e.,

$$\tilde{\rho}_{lum}(x) = \sum_{k=-K}^{K} \tilde{\rho}_k(x) \tag{3.17a}$$

$$= \hat{\rho}(x) * h_{lum}(x) \tag{3.17b}$$

where

$$h_{lum}(x) = \sum_{k=-K}^{K} h_k(x) \tag{3.18}$$

Eq. 3.18 follows from the linearity of the convolution operation. Once again, $\hat{\rho}(x)$ can be reconstructed via deconvolution:

$$\hat{\rho}(x) = \tilde{\rho}_{lum}(x) *^{-1} h_{lum}(x) \tag{3.19}$$

This extension of the method is called as Lumped-PCI.

While Lumped-PCI boosts SNR and improves noise robustness, it is slightly more sensitive against harmonic interferences when compared to PCI due to the usage of the pFOV edges. As seen in Fig. 3.2a, the reconstructed images using Eq. 3.16 for larger $|k|$ (i.e., using sampling positions near pFOV edges) exhibit accumulated error toward one end of the image. In contrast, Lumped-PCI image

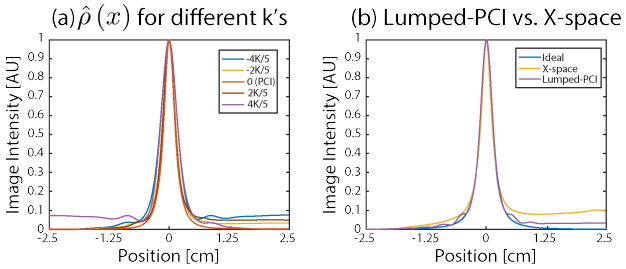

Figure 3.2: Effects of sampling position k on the MPI image reconstruction under harmonic interference. (a) The reconstructed images using Eq. 16 for different k's, where $k = 0$ image corresponds to PCI (i.e., using the centers of the pFOVs). As $|k|$ gets larger (i.e., using sampling positions near pFOV edges), the accumulated error toward one end of the image gets stronger. (b) The reconstructed images for Lumped-PCI vs. standard x-space reconstruction. Lumped-PCI provides interference robustness by effectively averaging out the negative/positive deviations from different k's, yielding only slight ripple-like artifacts.

in Fig. 3.2b shows only slight ripple-like artifacts. As Lumped-PCI sums the raw images from the entire pFOV, it effectively averages out the negative/positive deviations from the ideal values from different k's. Hence, Lumped-PCI still displays increased reconstruction fidelity and interference robustness when compared to standard x-space reconstruction.

3.3 Methods

3.3.1 Simulations

MPI simulations were carried out using a custom toolbox developed in MATLAB (Mathworks, Natick, MA). Simulation parameters were chosen to match the parameters of the in-house FFP MPI scanner (Fig. 3.3a). Accordingly, the selection field gradients were (-4.8, 2.4, 2.4) T/m/μ_0 in (x, y, z) directions. 10 mT drive field at 9.7 kHz along the z-direction was simulated together with a focus field that creates 1 T/s slew rate in the z-direction. A 5×5 cm^2 vasculature phantom was used, assuming 25 nm nanoparticle diameter. The pFOV size was 8.33 mm and a 2D FOV of 5×5 cm^2 was scanned using a linear trajectory, similar to the

one shown in Fig. 3.3b. The entire FOV was scanned in 51 lines. To match the conditions of the imaging experiments, the simulated MPI signal was sampled at 2 MS/s.

3.3.2 Noise and Harmonic Interference Robustness Analysis

To analyze the robustness of the proposed method, noise, harmonic interference, and relaxation effects were simulated on MPI signal. For noise analysis, white Gaussian noise was added to the time-domain MPI signal at 10 different noise levels, with signal-to-noise ratio (SNR) varying between 5-50 dB. SNR was defined using the peak signal amplitude as follows:

$$SNR = 20log_{10}\left(\frac{\max\limits_{t}\left|s\left(t\right)\right|}{\sigma}\right) \tag{3.20}$$

Here, σ denotes the standard deviation of noise, and $s\left(t\right)$ is the MPI signal after direct feedthrough filtering.

For harmonic interference analysis, harmonic interference was added to the spectrum of $s\left(t\right)$. When the drive field is applied alone, the spectrum of the MPI signal contains only the harmonics of the fundamental frequency, f_0 [15]. However, for the linear scan trajectory used in this work, the harmonics spread to very narrow nearby bands [27]. Let $S(f)$ denote the Fourier transform of $s(t)$ and $S_n(f)$ denote the n^{th} harmonic band, i.e.,

$$S_n(f) = \begin{cases} S(f) & , \left(n-\frac{1}{2}\right)f_0 < f < \left(n+\frac{1}{2}\right)f_0 \\ 0 & , \text{otherwise} \end{cases} \tag{3.21}$$

The magnitude of the interference added to the n^{th} harmonic (i.e., at $f = n\,f_0$) was uniformly distributed between 0 and γ_n, whereas the phase of it was uniformly distributed between 0 and 2π. To assess the strength of the MPI signal against harmonic interference, the signal-to-interference ratio (SIR) metric was

used. Based on experimental observations, harmonic interference was simulated so that each harmonic band had the same SIR level, i.e.,

$$SIR = 20log_{10}\left(\frac{\max\limits_{f}\left|S_n\left(f\right)\right|}{\gamma_n}\right) \tag{3.22}$$

Hence, as the magnitude spectrum in MPI decayed at higher harmonics, the interference followed the same trend. For simulations, 6 different SIR levels between 4-24 dB were tested.

First, noise and harmonic interference effects were simulated separately. Then, both effects were incorporated simultaneously with SNR ranging between 5-50 dB and SIR ranging between 4-24 dB. Monte Carlo simulations were performed via repeating each case 50 times. Next, to incorporate the effects of relaxation, a realistic time constant of $\tau = 3\ \mu s$ was utilized [28, 29], using the model provided in [30]. For this analysis, SNR was fixed at 30 dB and SIR at 8 dB.

3.3.3 Imaging Experiments

Imaging experiments were performed on in-house FFP MPI scanner (Fig. 3.3) [31]. The selection field of this scanner was generated by two permanent magnets with 7-cm diameter and 2-cm thickness, placed at 8-cm separation. The resulting selection field gradients were (-4.8, 2.4, 2.4) T/m/μ_0 in (x, y, z) directions. The drive field coil had a 1.5 mT/A sensitivity, with 95% homogeneity in a 4.5-cm long region, and was built using 3 layers of Litz wire with 80 turns. For the receive coil, a three-section gradiometer type coil with 34 and 17.5 windings for the main section and side sections was utilized [20]. The drive and receive coils were positioned coaxially, and placed inside a cylindrical copper shield with 1-cm thickness at the center of the magnet configuration. The maximum FOV of this FFP MPI scanner is 1×1×10 cm^3.

In imaging experiments, 0.7x7.52 cm^2 FOV in x-z plane was scanned. To cover this FOV, the linear trajectory shown in Fig. 3.3b was utilized. The drive field was at 9.7 kHz and 10 mT-peak along the z-direction, resulting in a 8.33 mm

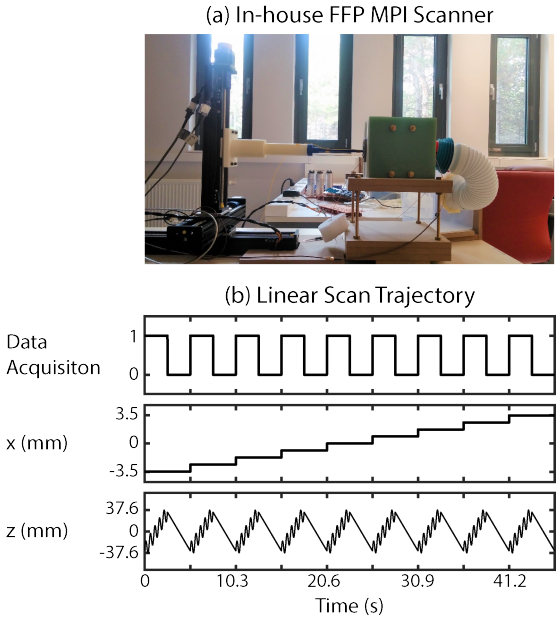

Figure 3.3: An overview of the in-house FFP MPI scanner and the linear scan trajectory used in the imaging experiments. (a) This scanner features (-4.8, 2.4, 2.4) T/m/μ_0 selection field gradients in (x, y, z) directions, with a maximum FOV of 1×1×10 cm^3. (b) The linear scan trajectory had 0.7×7.52 cm^2 FOV in x-z plane, 0.07 T/s slew rate along z-direction using continuous robotic arm motion, with 23.2 sec active scan time. This figure shows a simplified version of the actual trajectory: instead of the drive field at 9.7 kHz and 10 mT-peak, a representative drive field at a much lower frequency is plotted.

pFOV length. Instead of a focus field, a three-axis robotic arm (Motor-Driven Velmex BiSlide, Model: MN10-0100-E01-21) was used to move the phantom continuously along the z-direction, and stepwise along the x-direction. The maximum slew rate for the continuous motion was 0.07 T/s due to the speed limitation of this mechanical system. The entire FOV was scanned in 9 lines, with an active scan time of 23.2 sec.

3.3.4 Imaging Phantoms

Two different imaging phantoms were prepared to demonstrate the performance of the proposed method. For the first phantom, two 3-mm vials were filled with Perimag (Micromod GmbH, Germany) nanoparticles with a diluted concentration

of 5 mg Fe/mL. Vials were separated by 9-mm distance along the z-direction.

To show that the proposed method can successfully handle different nanoparticle types, a second phantom was prepared. For this phantom, three 2-mm inner diameter vials were filled with Nanomag-MIP (Micromod GmbH, Germany) nanoparticles with a diluted concentration of 1.43 mg Fe/mL, Vivotrax (Magnetic Insight Inc., USA) with an undiluted concentration of 5.5 mg Fe/mL, and a homogeneous mixture of the two. The vials were separated by 15-mm distances along the z-direction.

3.3.5 Signal Pre-processing & Image Reconstruction

The same signal pre-processing steps were used in both the simulations and experiments. First, the received signal was digitally high-pass filtered to remove any remaining direct feedthrough of the drive field. Next, for only experiments, a low-pass filter was applied to filter out the signal near and after the self-resonance frequency of the receive coil, which was measured at around 280 kHz. The resulting signal was further filtered for the purposes of spectrum cleaning. For the linear trajectories used in this work, pass-bands around the harmonics were defined, with a bandwidth of 420 Hz for simulations. Due to the relatively slower slew rate in the experiments, the signal spread to a narrow band around the harmonics. Therefore, a smaller pass-band bandwidth of 16 Hz was utilized for the experiments.

For PCI and Lumped-PCI, the pre-processed signal values were directly used to form the raw images, as described in Eq. 3.11a. Then, these images were interpolated to a finer grid of 0.05-mm spacing and deconvolved by the kernels computed from Eq. 3.8 and Eq. 3.18, taking $\beta_0 = 1$. The deconvolution was performed using the built-in MATLAB function *deconvreg*, to reconstruct the final MPI images. Here, *deconvreg* implements a regularized filter algorithm that finds the least squares estimate under image smoothness constraint.

3.3.6 Comparison of Image Quality

Standard x-space reconstruction with DC recovery algorithm [9] and SNR optimized pFOV stitching [24] was implemented for comparison purposes. The comparison and proposed techniques used identical signal pre-processing steps, as described in Chapter 3.3.5.

For quantitative image quality assessment of the reconstructed images in simulations, the PSNR metric was employed:

$$PSNR\,(I) = 10log_{10}\big(\frac{R^2}{MSE}\big) \tag{3.23}$$

where

$$MSE = \frac{\sum_{M,N}\big(I[m,n] - I_{ref}[m,n]\big)^2}{MN} \tag{3.24}$$

Here, $I[m,n]$ is the reconstructed image, R is the peak value that a pixel can have, $I_{ref}[m,n]$ is the reference image, MSE is the mean-squared-error between the reconstructed image and the reference image, and images are of size $M \times N$. The phantom itself was used as the reference image, and all reconstructed images were individually normalized to [0 1] range. Accordingly, higher PSNR values indicate higher fidelity image reconstruction.

3.4 Results

3.4.1 Simulation Results

Figure 3.4 shows the results of the proposed and comparison reconstructions for a 5×5 cm^2 vasculature phantom for the ideal case, where noise, interference, and relaxation effects are neglected. Figure 3.4a-3.4c show the phantom, the PSF-blurred ideal MPI image, and the corresponding standard x-space reconstruction result. Figure 3.4d-3.4g show the results of Lumped-PCI and PCI reconstructions together with the corresponding raw images. In addition, Fig. 3.4h shows 1D cross-sections of the reconstructed images to facilitate visual comparison. For

this ideal case, all three methods yield visually similar images, particularly in the central regions of the FOV. A quantitative comparison of these images yields 13.4 dB, 13.5 dB, and 14.1 dB PSNR values for standard x-space, Lumped-PCI, and PCI, respectively. Although there is no visible difference between the reconstructed images, the PSNR values suggest that the PCI method is the most successful reconstruction method under ideal signal conditions.

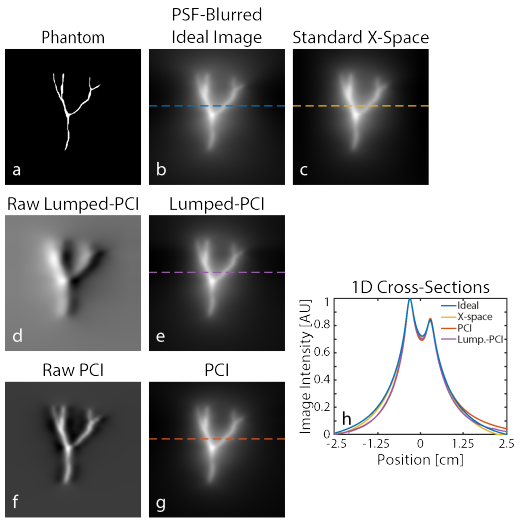

Figure 3.4: Simulation results for ideal signal conditions. (a) A 5×5 cm^2 vasculature phantom and (b) the corresponding PSF-blurred ideal MPI image. Images reconstructed using (c) standard x-space reconstruction, (e) Lumped-PCI, and (g) PCI. Here, (d) and (f) show the raw images for Lumped-PCI and PCI, respectively. (h) 1D cross-sections of the reconstructed images. Under ideal signal conditions, all three methods provide visually similar results.

Figure 3.5 shows example results for the proposed and comparison reconstructions at 4 different SNR levels between 10-40 dB. Both the standard x-space and Lumped-PCI methods display robustness against noise. For standard x-space, horizontal stripe artifacts appear for the lowest SNR level of 10 dB, stemming from the inconsistencies during the stitching operation for different lines in the image. In contrast, an overall blurring is visible at the same SNR level for Lumped-PCI, due to the trade-off between noise regularization and resolution. The PCI method, on the other hand, shows degradation in image quality for the lowest two SNR levels. This relative noise sensitivity is expected, as PCI uses only a small portion of the received signal.

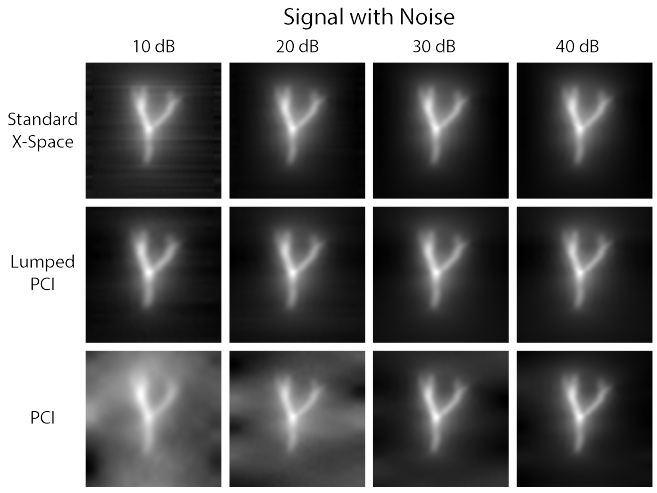

Figure 3.5: Example results at 4 different SNR levels between 10-40 dB. Both standard x-space and Lumped-PCI methods display robustness against noise, with slight horizontal stripe artifacts in standard x-space and an overall blurring in Lumped-PCI at very low SNR levels. PCI shows degradation in image quality for the lowest two SNR levels, as it uses only a small portion of the received signal.

Figure 3.6 shows example results at 4 different SIR levels between 4-16 dB. Standard x-space reconstruction displays sensitivity against harmonic interference, manifested as horizontal stripe artifacts that are visible even at the highest SIR level of 16 dB. While Lumped-PCI is considerably more robust against interference effects, similar but thicker horizontal stripes emerge at the lowest SIR level of 4 dB. In contrast, PCI demonstrates robustness against interference at all SIR levels tested. At the lowest SIR level, while there are image intensity differences in the background, these low-resolution features do not hinder the delineation of the phantom.

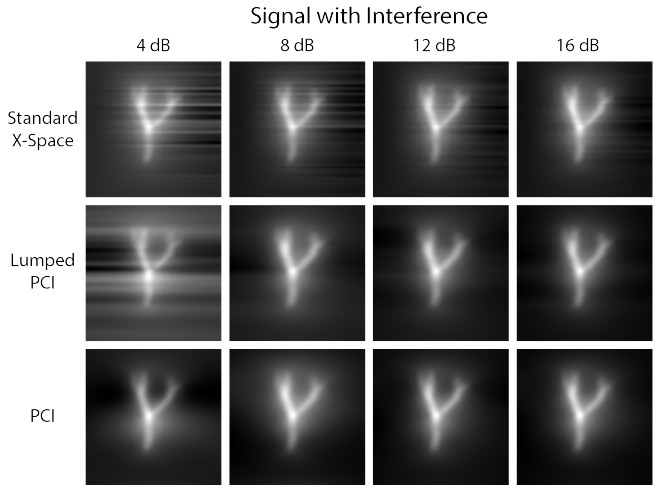

Figure 3.6: Example results at 4 different SIR levels between 4-16 dB. Standard x-space reconstruction suffers from horizontal stripe artifacts that are visible even at the highest SIR level of 16 dB. Lumped-PCI is more robust against interference effects, however, thicker horizontal stripe artifacts arise at the lowest SIR level of 4 dB. PCI demonstrates robustness against interference at all SIR levels.

Figure 3.7 displays the combined effects of noise and harmonic interference on the three reconstruction methods, at a fixed SIR level of 8 dB with SNR ranging between 10-40 dB. The presence of harmonic interference limits the performance of the standard x-space method, which suffers from stripe artifacts even at the highest SNR level of 40 dB. Lumped-PCI shows improved image quality at that SNR level, with relatively better behaved artifacts at lower SNR levels. In contrast, PCI shows almost no artifacts at the highest two SNR levels. However, its image quality degrades considerably for the lowest two SNR levels. These results are in line with those in Fig. 3.5 and Fig. 3.6. When noise is the dominant effect, Lumped-PCI performs the best, whereas when interference dominates over noise, PCI yields the highest image quality.

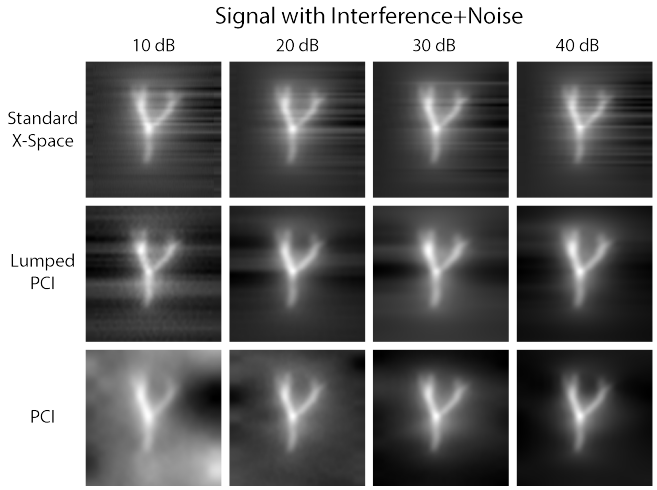

Figure 3.7: Example results at 4 different SNR levels between 10-40 dB, with SIR fixed at 8 dB. Due to harmonic interference, the standard x-space method exhibits stripe artifacts even at the highest SNR level of 40 dB. Lumped-PCI shows improved image quality at all SNR levels, with relatively better behaved artifacts. PCI shows almost no artifacts at the highest two SNR levels, whereas its image quality degrades for the lowest two SNR levels.

Next, the image qualities of the three methods were compared quantitatively using the PSNR metric. At each SNR and SIR level, Monte Carlo simulations were performed by repeating the simulations 50 times, and the resulting PSNR values were averaged across repeats. The contour plots of the mean PSNR values are shown in Fig. 3.8, where the individual effects of noise and harmonic interference are also provided (see SIR $= \infty$ and SNR $= \infty$ levels, respectively). According to this figure, the main factor that determines the performance of standard x-space is the interference level and not noise. Only for SNR < 20 dB, the performance depends jointly on the noise and interference levels. While the performance trends for Lumped-PCI are similar, it outperforms standard x-space at all SNR and SIR levels. The PSNR difference between Lumped-PCI and standard x-space increases as SNR and SIR decreases, e.g., the difference reaches 1.7 dB at SNR $= 10$ dB and SIR $= 4$ dB. As expected, with its robustness against interference, PCI outperforms standard x-space at moderate-to-high SNR levels (for SNR > 25 dB). PCI also outperforms Lumped-PCI when SNR > 30 dB. For example, at SNR $= 35$ dB and SIR $= 8$ dB, the PSNR values are 10.6 dB, 10.9 dB, and 12.0 dB for standard x-space, Lumped-PCI, and PCI, respectively. At low SNR levels, however, the performance of PCI quickly degrades, as noise effects dominate over interference.

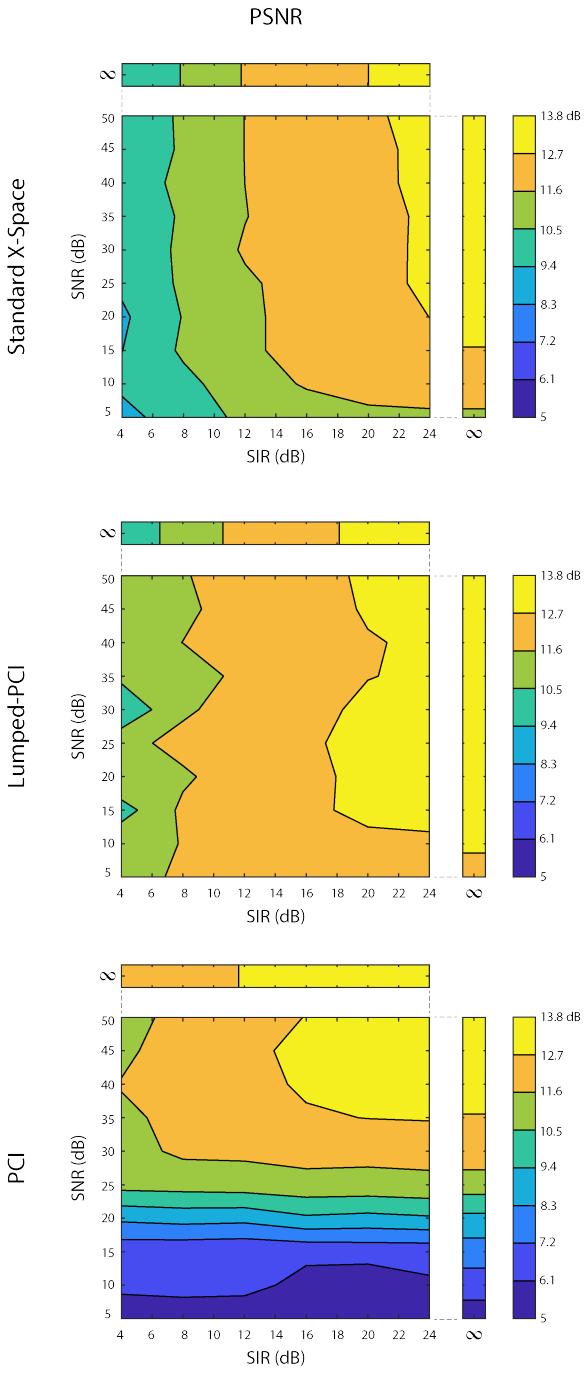

Figure 3.8: PSNR contour plots showing image quality as a function of SNR and SIR. The individual effects of noise and harmonic interference can be seen at SIR $= \infty$ and SNR $= \infty$ levels, respectively. The performance of standard x-space is mainly dependent on the interference level and not noise, except for SNR < 20 dB. Lumped-PCI outperforms standard x-space at all SNR and SIR levels. PCI yields the highest image quality when interference dominates over noise. PCI outperforms standard x-space when SNR > 25 dB, and Lumped-PCI when SNR > 30 dB.

Figure 3.9 displays the results of the proposed and comparison reconstructions for the combined effects of noise, interference, and relaxation. To investigate the effects of relaxation, a realistic relaxation time constant of $\tau = 3\ \mu s$ was assumed [28]. For this analysis, SNR was fixed at 30 dB and SIR at 8 dB. Comparing Fig. 3.9 with the third column of Fig. 3.7, one can see that relaxation causes a slight blurring for all three methods. The overall effects of noise and interference, however, remain the same as before. Once again, horizontal stripe artifacts are seen in the standard x-space image. Both Lumped-PCI and PCI provide improved image quality with respect to standard x-space. Under these specific conditions, PCI outperforms the other two methods. The PSNR values corresponding to standard x-space, Lumped-PCI, and PCI are 10.6 dB, 11.9 dB, and 12.6 dB, respectively.

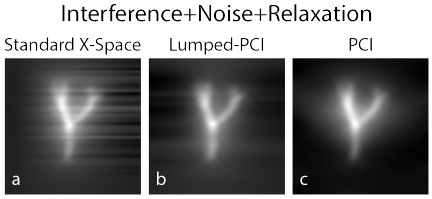

Figure 3.9: Simulation results for a realistic scenario where noise, harmonic interference, and relaxation effects are all incorporated: 30 dB SNR, 8 db SIR, relaxation time constant of $\tau = 3\ \mu s$. The MPI images reconstructed by (a) standard x-space, (b) Lumped-PCI, and (c) PCI exhibit a slight blurring due to relaxation, but the overall effects of noise and interference remain the same as in Fig. 3.7. Under these conditions, PCI provides the best image quality, whereas Lumped-PCI also shows improved quality when compared to standard x-space.

3.4.2 Imaging Experiment Results

Figure 3.10 displays the imaging experiment results of the proposed and comparison reconstructions using a phantom that contains two vials of Perimag nanoparticles separated by a 9-mm distance. Standard x-space suffers from a pile-up artifact in image intensity due to non-ideal signal conditions. Here, imaging experiments utilized 9 lines to cover the 2D FOV, as opposed to 51 lines used in the simulations. Therefore, the visual manifestation of the aforementioned horizontal stripe artifact is now a more dominant pile-up artifact. While Lumped-PCI also

demonstrates similar but less severe artifacts along the horizontal direction, the image quality is visibly improved when compared to standard x-space. On the other hand, PCI does not exhibit any artifacts and provides the highest image quality out of the three methods. Note that despite containing identical concentrations and volumes of the same nanoparticle, there is a visible intensity difference between the two vials for PCI, which potentially stems from an imperfect alignment of the phantom plane with respect to the 2D imaging plane. In standard x-space, the intensity difference is reversed because of the dominant pile-up artifact.

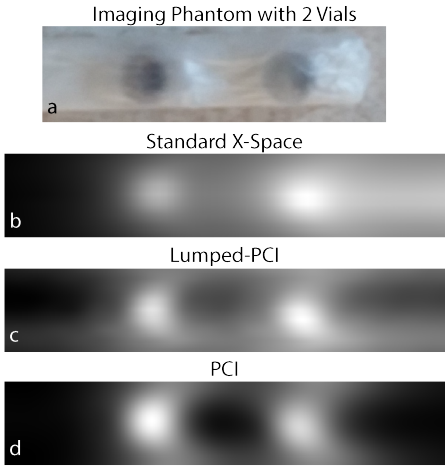

Figure 3.10: Experimental imaging results using (a) an imaging phantom with two vials filled with identical concentration of Perimag nanoparticles, separated at 9-mm distance. The reconstructed MPI images from (b) standard x-space, (c) Lumped-PCI, and (d) PCI. Standard x-space suffers from a pile-up artifact in image intensity due to non-ideal signal conditions, whereas Lumped-PCI provides improved image quality with similar but less severe artifacts along the horizontal direction. PCI does not exhibit any artifacts and provides the highest image quality out of the three methods. FOV size: 0.7×7.52 cm^2, displayed FOV size: 0.7×4.7 cm^2.

The experimental results in Fig. 3.11 show that the proposed methods can handle different nanoparticle types. Here, three vials filled with Nanomag-MIP, VivoTrax, and a homogeneous mixture of the two separated by 15-mm distances were imaged. Once again, standard x-space suffers from an intensity pile-up on the right hand side of the image. While the image quality of Lumped-PCI is improved with respect to standard x-space, the effects of interference can still be

observed in the horizontal direction. PCI is free from such artifacts and provides the highest image quality due to its robustness against harmonic interference effects.

For the experiments in Fig. 3.10 and 3.11, the SNR and SIR levels were computed from the MPI signals in time domain and frequency domain, respectively. These computations yielded SNR = 32.3 dB and SIR = 7.9 dB for the experiments in Fig. 3.10, and SNR = 31.1 dB and SIR = 4.8 dB for those in Fig. 3.11. The parameters for the simulations in Fig. 3.9 were based on these experimental results. One can see that the overall effects of non-ideal signal conditions in the experiments are consistent with those seen in the simulations. These proof-of-concept experiments demonstrate both the feasibility with different nanoparticle types and robustness against non-ideal signal conditions for the proposed methods.

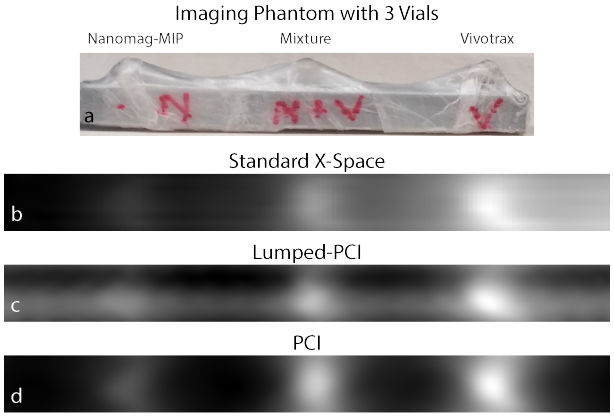

Figure 3.11: Experimental imaging results using different types of nanoparticles. (a) The imaging phantom of three vials filled with Nanomag-MIP, Vivotrax, and a homogeneous mixture of the two. The reconstructed MPI images from (b) standard x-space, (c) Lumped-PCI, and (d) PCI. PCI gives the highest image quality out of the three methods. The results show that the proposed methods can successfully handle different nanoparticle types. FOV size: 0.7×7.52 cm^2.

3.5 Discussion

In this chapter, with simulations and experimental results, it has been shown that PCI provides improved robustness against harmonic interferences when compared to standard x-space reconstruction. In cases where using only a small portion of the received signal renders PCI sensitive to noise, it is proposed to improve its noise robustness by lumping the signals from the entire pFOV. Utilizing the edges of the pFOVs reduces interference robustness of Lumped-PCI, hence, a clear trade-off between noise robustness and interference robustness emerges. To adjust to a specific SNR and SIR level, a central region of pFOV can be lumped instead of the entire pFOV. For example, the signals at pFOV edges can be discarded without significant data loss to improve interference robustness. Similarly, standard x-space reconstruction also proposed using the central 95% of pFOV to avoid velocity-compensation-induced noise amplification at the edges [9]. Note that while this procedure improves noise robustness of x-space reconstruction, it does not provide sufficient robustness against interference. In fact, the experimental results in Fig. 3.10b and Fig. 3.11b utilized the central 90% of pFOV for x-space reconstruction, but still exhibited pile-up artifacts.

There are multiple potential sources of harmonic interferences in MPI, most notably the non-linearities in the transmit chain (e.g., from power amplifier or capacitors). Especially if the active/passive compensation of the direct feedthrough does not provide sufficient decoupling between the transmit and receive coils, the higher harmonics of the drive field can also feed through to the MPI signal. In addition, insufficient shielding may cause eddy currents on the selection field permanent magnets, which in turn can induce signal on the receive coil [32, 33]. Likewise, ambient interferences may also become problematic due to insufficient shielding of the receive coil and/or transmit/receive filter chains [34]. Under low signal conditions, such as *in vivo* cases, these harmonic interferences can become a problem even for well-tuned systems. Therefore, the reconstruction technique proposed in this work can improve image quality not just for low-cost MPI scanners (e.g., like the FFP scanner used in this work), but also for high-fidelity

commercial systems. Moreover, the proposed PCI method substantially simplifies the reconstruction procedure by eliminating the need for individual pFOV processing (i.e., gridding, DC shift calculation, and stitching).

It should be emphasized that while the proposed method is demonstrated for linear trajectories, it is applicable to any trajectory that contains a 1D drive field with a slowly varying focus field. The sizes of the kernels in Eqs. 3.8 and 3.18 become more compact at smaller drive field amplitudes, which would yield a higher fidelity deconvolution with reduced noise-amplification effects. One of the aforementioned requirements of PCI is that the pFOV centers are closely spaced, such that there are multiple samples per kernel length W (i.e., the pFOV extent). Note that this requirement can be thought to be identical to the overlapping pFOV requirement of standard x-space reconstruction. Nevertheless, due to the 20 T/s safety limit on the slew rate of the focus field [14], realistic scan trajectories must already consist of closely spaced pFOVs. For the experiments in this work, using a drive field at 9.7 kHz with a slew rate of 70 mT/s yielded 3-μm distances between pFOV centers. This level of spacing is more than sufficient to reconstruct a high quality image, as it is three orders of magnitude below the expected mm-range resolution of the in-house scanner and is well below typical pFOV sizes. When operating at the safety limit of 20 T/s slew rate [14], the distances between pFOV centers would scale up to 0.86 mm. While this spacing may also be sufficient in most cases, the slew rate of the focus field can be reduced accordingly to attain a desired spacing level. Demonstration of PCI at such high slew rates remains as future work, as it requires incorporating electromagnetically driven focus fields.

The compact kernels used in PCI and Lumped-PCI both have fully-known shapes that solely depend on the pFOV size. The scaling factor β_0, however, depends on the nanoparticle type. Using a constant β_0 (as done in this work) results in a global scaling of the reconstructed image for cases with a single type of nanoparticle, and nanoparticle-dependent scaling of pixel intensities for cases with more than one type of nanoparticle. It is important to note that an identical scaling effect is also present in standard x-space reconstruction, as the speed compensation step does not correct for the nanoparticle-dependent parameter α in Eq. 3.1. Nevertheless, in the case of single type of nanoparticle, the benign global

scaling can easily be corrected by imaging a source with known concentration and rescaling other images respectively. For cases with more than one type of nanoparticle, one potential solution to correct for nanoparticle-dependent scaling is to measure the relative values of β_0 by performing a calibration scan using point sources of identical concentrations. Note that this measurement could also be performed on a magnetic particle spectrometer (MPS) setup, as the relative scaling of β_0 values is independent of the system parameters. One can then determine the spatial distribution of each nanoparticle type using multi-color MPI techniques [35, 28], and achieve true pixel intensities via local rescaling of the reconstructed image by the relative β_0 values. Demonstration of this approach remains an important future extension of the proposed PCI method.

The proposed method also has the potential to be combined with some of the recently proposed x-space reconstruction approaches. A recent work has shown that one can achieve isotropic resolution with standard x-space reconstruction by combining images from two orthogonal scanning directions [36]. The resolution of the resulting isotropic image can then be further improved by using an equalization filter that extracts the image component stemming from the narrower tangential PSF [37, 18]. By replacing the standard x-space reconstruction step with PCI, the harmonic interference robustness of these multi-channel acquisition and equalization approaches can be significantly improved. Another recent work proposed a hybrid method that combines an x-space-based reconstruction with a system function approach [38]. This method first uses a gridding based reconstruction to generate a raw image, followed by an image-based system matrix reconstruction to correct for system-induced geometric warping and position-dependent blurring effects. Likewise, a hybrid extension of PCI that incorporates system function reconstruction could also be pursued to gain robustness against magnetic field inhomogeneities of an MPI scanner, along with the robustness against harmonic interferences.

Chapter 4

Harmonic Dispersion X-space (HD-X) Reconstruction for Rapid Scanning Trajectories in MPI

4.1 Introduction

This chapter proposes an alternative approach to overcome the direct feedthrough problem in MPI. This alternative approach also gives rise to a streamlined reconstruction without overlap requirement among pFOVs. This approach takes advantage of the dispersion of the harmonics into nearby bands under the presence of time-varying focus fields. A sharp band-stop filter around the first harmonic eliminates the direct feedthrough, while dispersion prevents a complete loss of the information in the fundamental frequency band. A subsequent sampling of the filtered signal provides a straightforward reconstruction without pFOV processing steps, called as harmonic dispersion x-space (HD-X) reconstruction. Importantly, since it does not employ any DC recovery algorithm, HD-X does not require the

pFOV to overlap, unlike standard x-space reconstruction. Therefore, HD-X is applicable to sparse trajectories where standard x-space reconstruction cannot be applied. The proposed reconstruction can also be combined with standard x-space reconstruction by incorporating the speed compensation step, but eliminating the DC recovery step. Here, this hybrid method is referred to as hybrid HD-X. The performances of the proposed and standard x-space reconstructions are analyzed via extensive simulations and imaging experiments. The results show that the proposed methods outperform the standard x-space reconstruction in terms of image quality and noise robustness, while also enabling high-fidelity x-space reconstructions of rapid and sparse trajectories with non-overlapping pFOVs.

4.2 Theory

4.2.1 Harmonic Dispersion X-Space (HD-X) Reconstruction

This chapter assumes a trajectory that consists of a 2D focus field in x-z plane and a 1D drive field in z-direction. Then, the multidimensional time-domain MPI signal given in Eq. 2.11 can be re-written as [15, 16]:

$$s(t) = \alpha \left\| \dot{\mathbf{x}}_{\mathbf{s}}(t) \right\| IMG\big(\mathbf{x}_{\mathbf{s}}(t)\big) \tag{4.1}$$

where

$$IMG\big(\mathbf{x}_{\mathbf{s}}(t)\big) = \rho(\mathbf{x}) * * * \hat{\dot{\mathbf{x}}}_{\mathbf{s}} \cdot \mathbf{h}(\mathbf{x}) \hat{\dot{\mathbf{x}}}_{\mathbf{s}} \big|_{x=\mathbf{x}_{\mathbf{s}}(t)} \tag{4.2}$$

Here, $\rho(\mathbf{x})$ is the spatial distribution of nanoparticles, $\mathbf{h}(\mathbf{x})$ is the point spread function, $\mathbf{x}_{\mathbf{s}}(t)$ is the FFP position, $\dot{\mathbf{x}}_{\mathbf{s}}(t)$ is the FFP velocity, $\hat{\dot{\mathbf{x}}}_{\mathbf{s}}(t)$ is the unit vector along the same direction, and α is a constant.

If piece-wise constant focus fields in x- and z-directions are applied together with a sinusoidal drive field along z-direction, the FFP trajectory can be written as:

$$\mathbf{x}_{\mathbf{s}}(t) = \begin{bmatrix} x_i \\ \frac{W}{2} cos(\omega_0 t) + z_i \end{bmatrix} \tag{4.3}$$

where (x_i, z_i) is the center of the i^{th} pFOV, W is the extent of the pFOV, and ω_0 is the frequency of the drive field. Since $\mathbf{x_s}(t)$ is periodic, $s(t)$ is also periodic. As a result, the spectrum of $s(t)$ consists of only the harmonics of ω_0 [15]. For this trajectory, the direct feedthrough can be eliminated by filtering out the first harmonic via high-pass filtering, which is shown to cause a loss of different DC values for each pFOV [9]. Standard x-space reconstruction recovers these DC values by enforcing continuity among the overlapping portions of the pFOVs.

Instead of piece-wise constant focus fields, this work considers a rapid multi-dimensional trajectory that utilizes 2D continuous focus fields for covering an FOV in x-z plane:

$$\mathbf{x_s}(t) = \begin{bmatrix} \phi_x t \\ \frac{W}{2} cos(\omega_0 t) + \phi_z t \end{bmatrix} \tag{4.4}$$

Here, ϕ_x and ϕ_z are the speeds of the linear FFP movements induced by the focus fields in x- and z-directions, respectively. For this trajectory, $\mathbf{x_s}(t)$, and therefore $s(t)$, are no longer periodic. Breaking the periodicity results in the dispersion of the harmonics into nearby bands, as shown in Fig. 4.1.

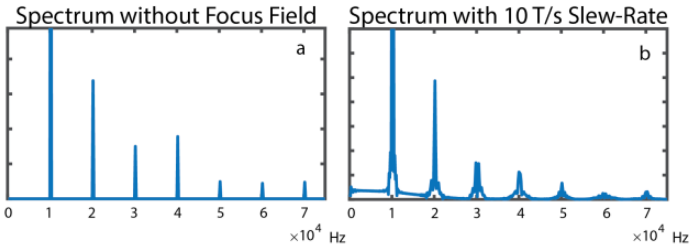

Figure 4.1: The dispersion of the harmonics into nearby bands under the presence of focus fields. Simulations were for a point source, 2.4 T/m/μ_0 selection field gradient, and a 10 mT drive field at 9.7 kHz.

It is important to note that, While the harmonics of the signal are dispersed, the direct feedthrough is still restricted to ω_0. For such a spectrum, a sharp band-stop filter at ω_0 can be utilized to eliminate the direct feedthrough, while preserving some of the information dispersed into the first harmonic band. Expressing the lost component as a sinusoid at frequency ω_0, the filtered signal can be written as follows:

$$s_{FOV}(t) = \alpha \left\| \dot{\mathbf{x}}_\mathbf{s}(t) \right\| IMG\big(\mathbf{x_s}(t)\big) - \gamma sin(\omega_0 t + \theta) \tag{4.5}$$

Here, γ and θ are the unknown amplitude and phase of the lost component. Next, if one samples this signal with a sampling period $T = \frac{2\pi}{\omega_0}$:

$$s_{FOV}[n] = s_{FOV}(nT + \Delta t) = \beta\ IMG(\mathbf{x_s}[n])) - \hat{\gamma} \tag{4.6}$$

where

$$\mathbf{x_s}[n] = \begin{bmatrix} \phi_x nT \\ \Delta x + \phi_z nT \end{bmatrix} \tag{4.7}$$

Here, Δt represents a potential timing offset in sampling, and $\hat{\gamma}$, β, and Δx are constants. Importantly, after sampling, the loss due to filtering becomes a DC term $\hat{\gamma}$, which is constant for the *entire* FOV. If the FOV is sufficiently large, $\hat{\gamma}$ can be determined by enforcing non-negativity on the final image. Then, one can easily obtain the ideal MPI image from the sampled filtered signal:

$$IMG(\mathbf{x_s}[n]) = \frac{s_{FOV}[n] + \hat{\gamma}}{\beta} \tag{4.8}$$

This proposed technique is called harmonic dispersion x-space (HD-X) reconstruction. HD-X does not employ pFOV processing, DC shift calculation, or pFOV stitching.

4.2.2 Hybrid HD-X

Due to the periodic sampling step, HD-X uses only a small portion of the received signal, which can cause two potential problems: sensitivity against noise and lower resolution for sparse trajectories. To overcome these problems, a modified version of the HD-X is proposed, which uses all of the received signal. This method first performs velocity compensation on the filtered signal:

$$\frac{s_{FOV}(t)}{\alpha\left\|\dot{\mathbf{x}}_\mathbf{s}(t)\right\|} = \frac{\alpha\left\|\dot{\mathbf{x}}_\mathbf{s}(t)\right\| IMG\big(\mathbf{x_s}(t)\big) - \gamma sin(\omega_0 t + \theta)}{\alpha\left\|\dot{\mathbf{x}}_\mathbf{s}(t)\right\|} \tag{4.9a}$$

$$\approx IMG\big(\mathbf{x_s}(t)\big) - \frac{\gamma sin(\omega_0 t + \theta)}{\alpha\big| - \frac{W}{2}\omega_0 sin(\omega_0 t) + \phi_z\big|} \tag{4.9b}$$

$$\approx IMG\big(\mathbf{x_s}(t)\big) - \frac{\gamma sin(\omega_0 t + \theta)}{\alpha\big| - \frac{W}{2}\omega_0 sin(\omega_0 t)\big|} \tag{4.9c}$$

Equation 4.9b follows from the fact that, for the majority of the trajectory, the FFP speed is dominated by the drive field along the z-direction. Therefore, one can safely ignore the x-component of $\dot{\mathbf{x}}_\mathbf{s}(t)$ when calculating its norm. Likewise, assuming that $|\frac{W}{2}\omega_0 sin(\omega_0 t)| >> |\phi_z|$, which is valid in the central regions of the pFOVs, one can ignore the speed term due to the x-component of focus field as done in Eq. 4.9c. Next, considering only the positive scanning direction of the drive field, i.e., for $-\frac{W}{2}\omega_0 sin(\omega_0 t) > 0$, one can write:

$$\frac{s_{FOV}(t)}{\alpha\|\dot{\mathbf{x}}_\mathbf{s}(t)\|} \approx IMG\big(\mathbf{x}_\mathbf{s}(t)\big) + \frac{\gamma sin(\omega_0 t + \theta)}{\alpha\frac{W}{2}\omega_0 sin(\omega_0 t)} \tag{4.10a}$$

$$\approx IMG\big(\mathbf{x}_\mathbf{s}(t)\big) + \frac{2\gamma\big(sin(\omega_0 t)(1 - \frac{\theta^2}{2}) + cos(\omega_0 t)\theta\big)}{\alpha W\omega_0 sin(\omega_0 t)} \tag{4.10b}$$

$$\approx IMG\big(\mathbf{x}_\mathbf{s}(t)\big) + \frac{2\gamma(1 - \frac{\theta^2}{2})}{\alpha W\omega_0} \tag{4.10c}$$

$$\approx IMG\big(\mathbf{x}_\mathbf{s}(t)\big) + \gamma' \tag{4.10d}$$

where

$$\gamma' = \frac{2\gamma(1 - \frac{\theta^2}{2})}{\alpha W\omega_0} \tag{4.11}$$

Here, Eq. 4.10b follows from sine summation relation and a small angle approximation for θ. Next, Eq. 4.10c was derived using the fact that $|sin(\omega_0 t)(1-\frac{\theta^2}{2})| >> |cos(\omega_0 t)\theta|$ in the central regions of the pFOVs. Following these derivations, Eq. 4.10d shows that the speed compensated signal is the ideal image with an additional DC term γ', which is constant for the *entire* FOV. This speed compensated signal can then be gridded to the FFP trajectory. Here, the constant γ' depends on the MPI system and the FFP trajectory, as well as the nanoparticle properties. It can be either calculated or set so that the minimum image intensity becomes zero. So, in a similar fashion as in HD-X, the ideal MPI image can be obtained as:

$$IMG\big(\mathbf{x}_\mathbf{s}(t)\big) = \frac{s_{FOV}(t)}{\alpha\|\dot{\mathbf{x}}_\mathbf{s}(t)\|} - \gamma' \tag{4.12}$$

Note that this extension of the HD-X again does not employ DC shift calculation, and therefore does not require overlaps among pFOVs. However, due to the speed compensation step, it can be considered as a combination of HD-X and standard x-space reconstruction. Hence, this technique is called as hybrid HD-X.

4.3 Methods

4.3.1 Simulations

MPI simulations were performed in MATLAB (Mathworks, Natick, MA). Simulation parameters were chosen to be identical with the parameters of the in-house MPI scanner. (-4.8, 2.4, 2.4) T/m/μ_0 selection field gradients in (x, y, z) directions, a 10 mT drive field at 9.7 kHz along z-direction, and a continuous 2D focus field in x-z plane with a resulting slew rate of 10 T/s were utilized. The entire 5×5 cm^2 FOV was covered using three different rapid 2D scan trajectories, as shown in Fig. 4.2. These trajectories differ from each other in terms of density. They cover the FOV in 100, 50, and 10 line segments, respectively. The least dense trajectory features non-overlapping pFOVs. As a phantom, a vasculature structure filled with nanoparticles of 25 nm diameter was used.

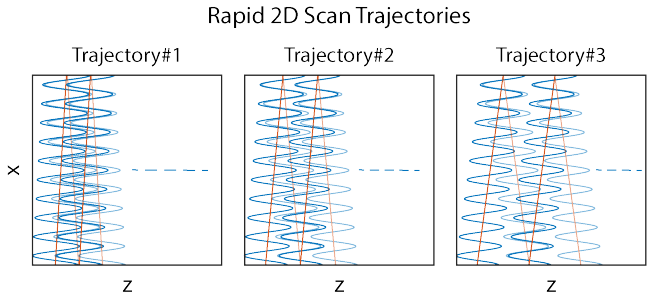

Figure 4.2: Schematics of rapid 2D scan trajectories used in simulations (actual trajectories were denser than shown). The trajectories used in the simulations cover the FOV in 100, 50, and 10 line segments, respectively. The least dense trajectory features non-overlapping pFOVs.

4.3.2 Noise Analysis

Noise effects were simulated on the MPI signal to analyze the noise robustness of the proposed and comparison techniques. For this analysis, white Gaussian noise was added to the time-domain MPI signal at 12 different SNR levels, from -5 dB to 50 dB. Denoting the standard deviation of noise as σ and the filtered

MPI signal as $s(t)$, SNR was defined as follows:

$$SNR = 20log_{10}\left(\frac{\max\limits_{t}\left|s\left(t\right)\right|}{\sigma}\right) \tag{4.13}$$

Monte Carlo simulations were performed by repeating the simulations at each SNR level 30 times.

4.3.3 Imaging Experiments

Imaging experiments were performed on the in-house MPI scanner (Fig. 4.3a-b) [31] whose design and operating specifications were given in Chapter 3.3.3 of this thesis. A 10 mT-peak drive field at 9.7 kHz was employed. Importantly, in contrast to the previous chapter, a rapid 2D scan trajectory was utilized for the experiment in this chapter. Accordingly, a 0.7×6 cm^2 FOV was covered by a rapid 2D scan trajectory shown in Fig. 4.3c. A robotic arm was used instead of electromagnetically driven focus fields. The speed of the robotic arm was 2.54 cm/s and the total scan time was 4.7 sec. This trajectory features non-overlapping pFOVs near the peripheries of the FOV. An imaging phantom with two 3-mm diameter vials, both filled with Perimag nanoparticles (Micromod, GmbH, Germany) of 5 mg Fe/mL concentration and separated at 2-cm distance, was imaged.

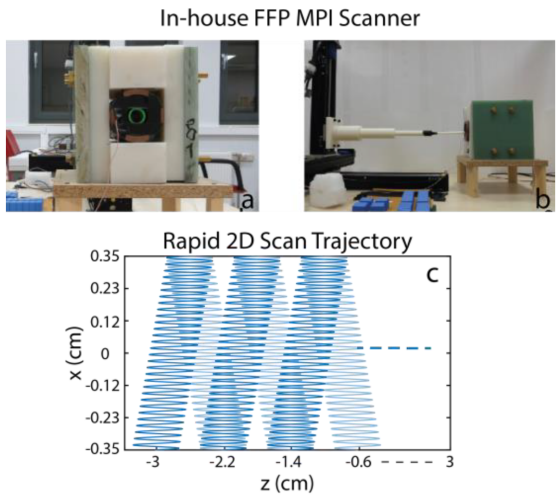

Figure 4.3: In-house MPI scanner: (a) front and (b) side views, and (c) the rapid 2D scan trajectory used for the imaging experiments. This trajectory features non-overlapping pFOVs near the peripheries of the FOV.

4.3.4 Comparison of Image Quality

The proposed methods were compared with standard x-space reconstruction with DC recovery algorithm and SNR optimized pFOV stitching [9, 24]. The PSNR metric was utilized to quantitatively assess the qualities of the reconstructed images in simulations:

$$PSNR\,(I) = 10log_{10}\big(\frac{R^2}{MSE}\big) \tag{4.14}$$

where

$$MSE = \frac{\sum_{M,N}\big(I[m,n] - I_{ref}[m,n]\big)^2}{MN} \tag{4.15}$$

Here, R is the maximum value a pixel can have, $I[m,n]$ and $I_{ref}[m,n]$ are the reconstructed and the reference images, MSE is the mean-squared-error between the two images, and the images are of size $M \times N$. The ideal MPI image (the phantom convolved with the PSF) was used as the reference image. For each method, the reconstructed images were normalized using the minimum and maximum pixel intensities of the image reconstructed under ideal signal conditions (i.e., noise-frees signal). Here, higher PSNR values indicate higher quality image reconstruction.

4.4 Results

4.4.1 Simulation Results

Figure 4.4 shows the simulation results for a vasculature phantom using three different trajectories, under ideal signal conditions. For Trajectory #1 and Trajectory #2, all three methods yield visually similar results. Note that standard x-space reconstruction was not applicable to Trajectory #3, since it utilizes non-overlapping pFOVs. Because it uses a small portion of the received signal, HD-X result for this trajectory has visibly low resolution, as one might expect. On the other hand, hybrid HD-X retains a high image quality even for this sparse trajectory.

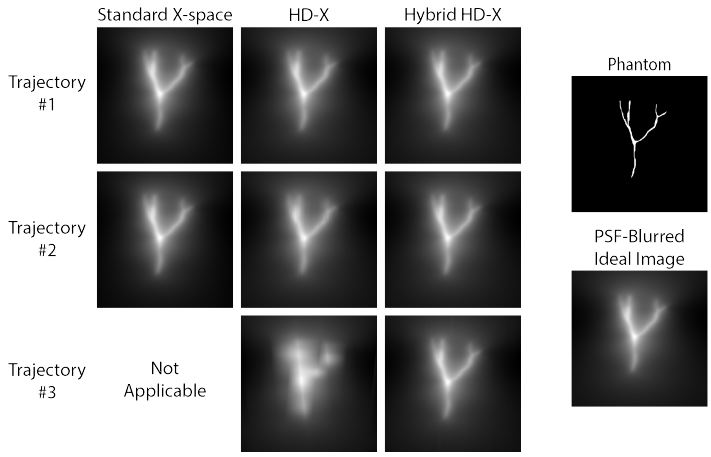

Figure 4.4: Simulation results under ideal signal conditions for three different trajectories with different densities. For the higher density trajectories (Trajectory #1 and Trajectory #2), all three methods yield visually similar results. For Trajectory #3, standard x-space is not applicable, since the trajectory includes non-overlapping pFOVs. Due to the sparse nature of this trajectory, HD-X exhibits visibly low resolution. However, hybrid HD-X provides high image quality reconstruction even for this sparse trajectory.

Figure 4.5 shows example images for Trajectory #1 at 4 different SNR levels between 10-40 dB. For the highest two SNR levels, all three methods perform similarly. However, for low SNR cases, standard x-space and HD-X methods exhibit artifacts. Especially the HD-X result for the lowest SNR level of 10 dB

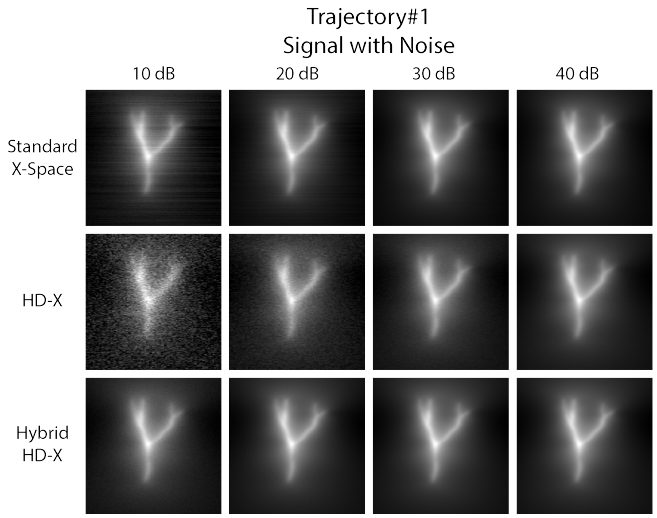

Figure 4.5: Example images for Trajectory #1 at 4 different SNR levels between 10-40 dB. Both standard x-space and HD-X methods exhibit noise-induced artifacts at low SNR levels. In contrast, hybrid HD-X is robust against noise and does not exhibit any artifacts even for the lowest SNR level of 10 dB.

is adversely affected by noise, which stems from the fact that the technique uses a small portion of the received signal. The standard x-space result for the same SNR level also exhibits stripe-like artefacts, caused by the DC recovery algorithm. In contrast, hybrid HD-X displays robustness against noise, and provides a high quality image even for the lowest SNR level of 10 dB.

Figure 4.6 shows example images for Trajectory #2 at 4 different SNR levels between 10-40 dB SNR. Again, for SNR levels greater than 30 dB, all three methods perform similarly, while standard x-space and HD-X methods this time exhibit slightly worse artifacts for lower SNR levels. Once again, hybrid HD-X performs well for all the SNR levels without any visible artifacts.

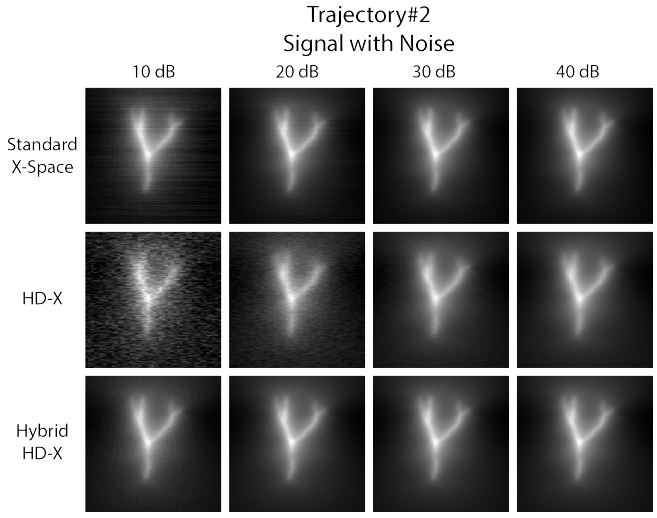

Figure 4.6: Example images for Trajectory #2 at 4 different SNR levels between 10-40 dB. Standard x-space and HD-X methods suffer due to noise at low SNR levels, while hybrid HD-X performs well for all the SNR levels.

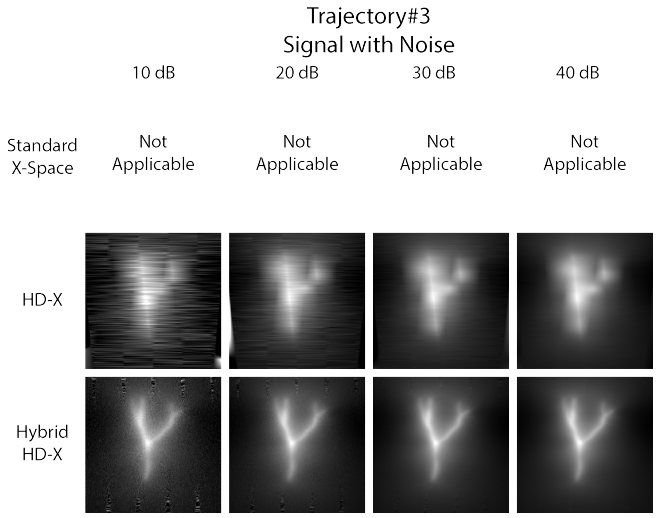

Figure 4.7: Example results for the most sparse Trajectory #3 at 4 different SNR levels between 10-40 dB. Standard x-space is not applicable due to the non-overlapping pFOVs utilized in this trajectory. Due to the sparsity of the trajectory, HD-X suffers from low resolution at all SNR levels, with further artifacts at low SNR levels. Hybrid HD-X also exhibits noise induced artifacts at the lowest two SNR levels in the peripheries of the FOV where the pFOVs are non-overlapping. Nonetheless, hybrid HD-X displays improved robustness against noise and high fidelity image reconstruction at all SNR levels.

Figure 4.7 shows example results for Trajectory #3 at 4 different SNR levels between 10-40 dB. Due to the non-overlapping pFOVs, standard x-space reconstruction is not applicable for this sparse trajectory. HD-X and hybrid HD-X, however, are still applicable. Due to the sparse nature of the trajectory, the subsampling operation in HD-X technique causes the resulting images to have visibly low resolution at all SNR levels. On the other hand, hybrid HD-X provides almost the same resolution as it does for the denser trajectories. Another manifestation of the trajectory sparsity is the noise-induced artifacts in HD-X that become more problematic at the lowest SNR level of 10 dB. Hybrid HD-X also exhibits artifacts for the lowest two SNR levels, in the peripheral regions of the FOV covered by non-overlapping pFOVs. Nevertheless, hybrid HD-X displays improved robustness against noise and high fidelity image reconstruction at all SNR level for this sparse trajectory.

Next, image qualities of the three methods were compared quantitatively using the PSNR metric. Figure 4.8 shows PSNR results from the Monte Carlo simulations for the aforementioned trajectories at 12 different SNR levels ranging between -5 and 50 dB, where simulations were repeated 30 times et each SNR level. Figure 4.8 shows the average PSNR values as a function of SNR. These results indicate that increasing trajectory density improves image quality for all three methods. For Trajectory #1, hybrid HD-X outperforms standard x-space at all SNR levels, whereas HD-X outperforms standard x-space for SNR levels greater than 15 dB. The results of Trajectory #2 display similar trends. For Trajectory #3 with non-overlapping pFOVs, standard x-space reconstruction is not applicable. On the other hand, for SNR levels greater than 20 dB, hybrid HD-X performs equally well for this sparse trajectory as it does for the other denser trajectories. For lower SNR levels, its performance is adversely affected by the sparsity of the trajectory. For this trajectory, the performance of HD-X degrades quickly at low SNR levels. Note that HD-X displays improved performance over standard x-space for the denser trajectories if the SNR level is greater than 25 dB. Overall, these results confirm the noise robustness and improved image quality of hybrid HD-X.

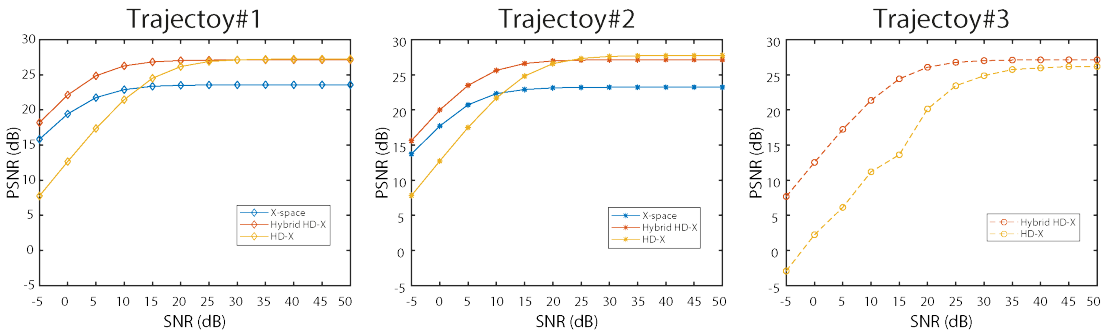

Figure 4.8: PSNR as a function of SNR, showing quantitative image quality comparison for different trajectories. Hybrid HD-X outperforms standard x-space for all three trajectories and at all SNR levels. HD-X also outperforms standard x-space at high SNR levels for all three trajectories. Moreover, hybrid HD-X retains high image quality for the sparse trajectory where standard x-space is not applicable.

4.4.2 Imaging Experiment Results

Figure 4.9 shows the imaging experiment results for a phantom with two vials filled with the same concentration of Perimag nanoparticles (Micromod, GmbH, Germany). The rapid and sparse 2D trajectory used in these imaging experiments utilized non-overlapping pFOVs. Therefore, standard x-space reconstruction was not applicable for the imaging experiments. On the other hand, proposed HD-X and hybrid HD-X methods are still applicable. As seen from the results, both methods provide high quality images despite the usage of non-overlapping pFOVs.

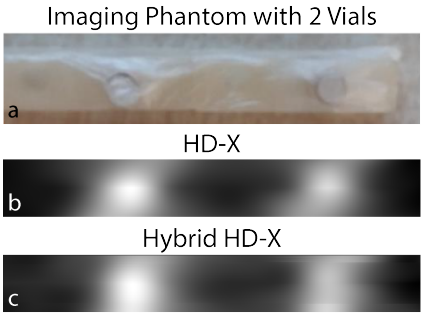

Figure 4.9: The imaging experiment results. (a) The imaging phantom with two vials filled with the same concentration of Perimag nanoparticles. MPI images reconstructed via (b) HD-X and (c) hybrid HD-X techniques, both displaying high fidelity image reconstructions for a trajectory with non-overlapping pFOVs. (FOV size: 0.7×6 cm^2)

4.5 Discussion

This chapter has shown with simulations and imaging experiments that HD-X can be successfully applied to trajectories where standard x-space reconstruction is not applicable due to the presence of non-overlapping pFOVs. HD-X offers a streamlined reconstruction by employing only a periodic sampling of the filtered signal followed by gridding. In the cases where this sampling causes resolution loss or sensitivity against noise, hybrid HD-X can be applied to obtain high quality MPI images for sparse trajectories.

The proposed methods not only enable x-space reconstruction of sparse trajectories, but also improve the reconstruction fidelity for dense trajectories. The reason is the elimination of the need for a DC recovery algorithm, which in turn renders HD-X based methods robust against noise. Extensive simulations show that hybrid HD-X outperforms standard x-space reconstruction at all SNR levels.

The proposed methods are based on the dispersion of the harmonics into nearby bands due to time-varying focus fields. For this work, sharp digital band-stop filters were utilized to eliminate the direct feedthrough for such a dispersed spectrum. If analog filters are utilized, the bandwidth and attenuation of the band-stop filter can affect the performance of the proposed HD-X based methods. On

the other hand, the amount of information that disperses to the side bands increases with increasing slew rate of the focus field. Therefore, for the higher slew rates of electromagnetically driven focus fields, the spectrum would become better suited for an analog band-stop filter at the fundamental frequency. An analysis of the effects of different filters on the reconstructed image remains as a future study.

Chapter 5

Conclusion

In this thesis, two novel x-space image reconstruction techniques were proposed: PCI and HD-X. The first technique, PCI, is a robust x-space image reconstruction that consists of two simplified steps: forming a raw image by directly assigning the signal to pFOV center locations, and deconvolving the raw image by a known, compact kernel. Extensive simulations and imaging experiments demonstrate that the proposed PCI method outperforms standard x-space reconstruction. PCI is particularly robust against harmonic interferences, making it a promising technique for *in vivo* applications. In SNR starved cases, the noise robustness of PCI can be further improved by lumping the signals from the entire pFOV, with a trade-off of slightly reduced interference robustness. The proposed method promises a computationally simpler and straightforward reconstruction with high-fidelity image reconstruction.

The second technique HD-X, is a streamlined x-space image reconstruction, which does not require overlapping pFOVs. This technique uses a sharp band-stop filter at the first harmonic followed by a periodic sampling of the signal to ensure that the information lost due to filtering is a constant DC term for the entire FOV. Since HD-X does not require the pFOVs to overlap, this solution is especially important for rapid and sparse scanning trajectories where standard x-space reconstruction is not applicable. A hybrid version of HD-X and the standard

x-space reconstruction was also shown to further improve the performance of the technique. Extensive simulations show that proposed HD-X and hybrid HD-X methods outperform standard x-space reconstruction.

The rapid and robust reconstruction techniques presented in this thesis remarkably improve the x-space reconstruction in terms of robustness against non-ideal signal conditions and image quality, while streamlining the reconstruction process and eliminating the need for overlapping pFOVs.

Bibliography

[1] B. Gleich and J. Weizenecker, "Tomographic imaging using the nonlinear response of magnetic particles," *Nature*, vol. 435, no. 7046, pp. 1214–1217, 2005.

[2] J. Weizenecker, J. Borgert, and B. Gleich, "A simulation study on the resolution and sensitivity of magnetic particle imaging," *Physics in Medicine and Biology*, vol. 52, no. 21, pp. 6363–6374, 2007.

[3] P. W. Goodwill, E. U. Saritas, L. R. Croft, T. N. Kim, K. M. Krishnan, D. V. Schaffer, and S. M. Conolly, "X-space MPI: Magnetic nanoparticles for safe medical imaging," *Advanced Materials*, vol. 24, no. 28, pp. 3870–3877, 2012.

[4] E. U. Saritas, P. W. Goodwill, L. R. Croft, J. J. Konkle, K. Lu, B. Zheng, and S. M. Conolly, "Magnetic particle imaging (MPI) for NMR and MRI researchers," *Journal of Magnetic Resonance*, vol. 229, pp. 116 – 126, 2013.

[5] L. M. Bauer, S. F. Situ, M. A. Griswold, and A. C. S. Samia, "Magnetic particle imaging tracers: State-of-the-art and future directions," *The Journal of Physical Chemistry Letters*, vol. 6, no. 13, pp. 2509–2517, 2015.

[6] B. Zheng, E. Yu, R. Orendorff, K. Lu, J. J. Konkle, Z. W. Tay, D. Hensley, X. Y. Zhou, P. Chandrasekharan, E. U. Saritas, P. W. Goodwill, J. D. Hazle, and S. M. Conolly, "Seeing SPIOs directly in vivo with magnetic particle imaging," *Molecular Imaging and Biology*, vol. 19, no. 3, pp. 385–390, 2017.

[7] E. U. Saritas, P. W. Goodwill, G. Z. Zhang, and S. M. Conolly, "Magnetostimulation limits in magnetic particle imaging," *IEEE Transactions on Medical Imaging*, vol. 32, no. 9, pp. 1600–1610, 2013.

[8] I. Schmale, B. Gleich, J. Rahmer, C. Bontus, J. Schmidt, and J. Borgert, "MPI safety in the view of MRI safety standards," *IEEE Transactions on Magnetics*, vol. 51, no. 2, pp. 1–4, 2015.

[9] K. Lu, P. W. Goodwill, E. U. Saritas, B. Zheng, and S. M. Conolly, "Linearity and shift invariance for quantitative magnetic particle imaging," *IEEE Transactions on Medical Imaging*, vol. 32, no. 9, pp. 1565–1575, 2013.

[10] M. Gruttner, T. F. Sattel, F. Griese, and T. M. Buzug, "System matrices for field of view patches in magnetic particle imaging," in *Proc. SPIE 8672, Medical Imaging 2013: Biomedical Applications in Molecular, Structural, and Functional Imaging*, vol. 8672, p. 86721A, 2013.

[11] P. Szwargulski, M. Ahlborg, C. Kaethner, and T. M. Buzug, "Trajectory analysis using static patches for magnetic particle imaging," *IEEE Transactions on Magnetics*, vol. 51, no. 2, pp. 1–4, 2015.

[12] T. Knopp and M. Kaul, "MPI focus field experiments using non-overlapping focus-field patches," in *Proc. 5th International Workshop on Magnetic Particle Imaging (IWMPI)*, pp. 1–1, Mar. 2015.

[13] J. J. Konkle, P. W. Goodwill, E. U. Saritas, B. Zheng, K. Lu, and S. M. Conolly, "Twenty-fold acceleration of 3D projection reconstruction MPI," *Biomedizinische Technik. Biomedical engineering*, vol. 58, no. 6, pp. 565–576, 2013.

[14] International Commission on Non-Ionizing Radiation Protection (ICNIRP), "Medical magnetic resonance (MR) procedures: protection of patients," *Health Phys*, vol. 87, no. 2, pp. 197–216, 2004.

[15] P. W. Goodwill and S. M. Conolly, "The x-space formulation of the magnetic particle imaging process: 1-D signal, resolution, bandwidth, SNR, SAR, and magnetostimulation," *IEEE Transactions on Medical Imaging*, vol. 29, no. 11, pp. 1851–1859, 2010.

[16] P. W. Goodwill and S. M. Conolly, "Multidimensional x-space magnetic particle imaging," *IEEE Transactions on Medical Imaging*, vol. 30, no. 9, pp. 1581–1590, 2011.

[17] J. J. Konkle, P. W. Goodwill, D. W. Hensley, R. D. Orendorff, M. Lustig, and S. M. Conolly, "A convex formulation for magnetic particle imaging x-space reconstruction," *PLOS ONE*, vol. 10, no. 10, p. e0140137, 2015.

[18] A. A. Ozaslan, A. Alacaoglu, O. B. Demirel, T. Çukur, and E. U. Saritas, "Fully automated gridding reconstruction for non-cartesian x-space magnetic particle imaging," *Physics in Medicine & Biology*, vol. 64, no. 16, p. 165018, 2019.

[19] Z. W. Tay, D. Hensley, J. Ma, P. Chandrasekharan, B. Zheng, P. Goodwill, and S. Conolly, "Pulsed excitation in magnetic particle imaging," *IEEE Transactions on Medical Imaging*, vol. 38, no. 10, pp. 2389–2399, 2019.

[20] M. Utkur and E. U. Saritas, "Comparison of different coil topologies for an MPI relaxometer," in *Proc. 5th International Workshop on Magnetic Particle Imaging (IWMPI)*, pp. 1–1, Mar. 2015.

[21] P. W. Goodwill, J. J. Konkle, B. Zheng, E. U. Saritas, and S. M. Conolly, "Projection x-space magnetic particle imaging," *IEEE Transactions on Medical Imaging*, vol. 31, no. 5, pp. 1076–1085, 2012.

[22] M. Graeser, T. Knopp, M. Grüttner, T. F. Sattel, and T. M. Buzug, "Analog receive signal processing for magnetic particle imaging," *Medical Physics*, vol. 40, no. 4, p. 042303, 2013.

[23] D. Pantke, N. Holle, A. Mogarkar, M. Straub, and V. Schulz, "Multifrequency magnetic particle imaging enabled by a combined passive and active drive field feed-through compensation approach," *Medical Physics*, vol. 46, no. 9, pp. 4077–4086, 2019.

[24] E. Bozkurt and E. U. Saritas, "Signal-to-noise ratio optimized image reconstruction technique for magnetic particle imaging," *J. Fac. Eng. Archit. Gaz.*, vol. 32, pp. 999–1013, 2017.

[25] J. Rahmer, J. Weizenecker, B. Gleich, and J. Borgert, "Signal encoding in magnetic particle imaging: Properties of the system function," *BMC medical imaging*, vol. 9, p. 4, 2009.

[26] D. Sarica, O. B. Demirel, and E. U. Saritas, "DC shift based image reconstruction for magnetic particle imaging," in *Proc. 25th Signal Processing and Communications Applications Conference (SIU)*, pp. 1–4, May 2017.

[27] S. Kurt, Y. Muslu, M. Utkur, and E. U. Saritas, "Harmonic dispersion x-space MPI," in *Proc. 9th International Workshop on Magnetic Particle Imaging (IWMPI)*, pp. 75–76, Mar. 2019.

[28] Y. Muslu, M. Utkur, O. B. Demirel, and E. U. Saritas, "Calibration-free relaxation-based multi-color magnetic particle imaging," *IEEE Transactions on Medical Imaging*, vol. 37, no. 8, pp. 1920–1931, 2018.

[29] M. Utkur, Y. Muslu, and E. U. Saritas, "Relaxation-based color magnetic particle imaging for viscosity mapping," *Applied Physics Letters*, vol. 115, no. 15, p. 152403, 2019.

[30] L. R. Croft, P. W. Goodwill, and S. M. Conolly, "Relaxation in x-space magnetic particle imaging," *IEEE Transactions on Medical Imaging*, vol. 31, no. 12, pp. 2335–2342, 2012.

[31] M. Utkur, Y. Muslu, and E. U. Saritas, "A 4.8 T/m magnetic particle imaging scanner design and construction," in *Proc. 21st National Biomedical Engineering Meeting (BIYOMUT)*, pp. i–iv, Nov. 2017.

[32] P. W. Goodwill, K. Lu, B. Zheng, and S. M. Conolly, "An x-space magnetic particle imaging scanner," *Review of Scientific Instruments*, vol. 83, no. 3, p. 033708, 2012.

[33] D. M. Yalcinkaya, M. Utkur, and E. U. Saritas, "Finite element analysis of passive magnetic shields for a FFP MPI scanner," in *Proc. 8th Internationa Workshop on Magnetic Particle Imaging (IWMPI)*, pp. 123–124, Mar. 2018.

[34] L. M. Bauer, D. W. Hensley, B. Zheng, Z. W. Tay, P. W. Goodwill, M. A. Griswold, and S. M. Conolly, "Eddy current-shielded x-space relaxometer for sensitive magnetic nanoparticle characterization," *Review of Scientific Instruments*, vol. 87, no. 5, p. 055109, 2016.

[35] J. Rahmer, A. Halkola, B. Gleich, I. Schmale, and J. Borgert, "First experimental evidence of the feasibility of multi-color magnetic particle imaging," *Physics in Medicine and Biology*, vol. 60, no. 5, pp. 1775–1791, 2015.

[36] K. Lu, P. Goodwill, B. Zheng, and S. Conolly, "Multi-channel acquisition for isotropic resolution in magnetic particle imaging," *IEEE Transactions on Medical Imaging*, vol. 37, no. 9, pp. 1989–1998, 2018.

[37] K. Lu, P. Goodwill, B. Zheng, and S. Conolly, "Reshaping the 2D MPI PSF to be isotropic and sharp using vector acquisition and equalization," in *Proc. 5th International Workshop on Magnetic Particle Imaging (IWMPI)*, pp. 1–1, 2015.

[38] P. Vogel, T. Kampf, M. A. Ruckert, and V. C. Behr, "Flexible and dynamic patch reconstruction for traveling wave magnetic particle imaging," *International Journal on Magnetic Particle Imaging*, vol. 2, no. 2, p. 611001, 2016.